

Proteome profile of peripheral myelin in healthy mice and in a neuropathy model

Sophie B Siems^{1†}, Olaf Jahn^{2†}, Maria A Eichel¹, Nirmal Kannaiyan³,
Lai Man N Wu⁴, Diane L Sherman⁴, Kathrin Kusch¹, Dörte Hesse²,
Ramona B Jung¹, Robert Fledrich^{1,5}, Michael W Sereda^{1,6}, Moritz J Rossner³,
Peter J Brophy⁴, Hauke B Werner^{1*}

¹Department of Neurogenetics, Max Planck Institute of Experimental Medicine, Göttingen, Germany; ²Proteomics Group, Max Planck Institute of Experimental Medicine, Göttingen, Germany; ³Department of Psychiatry and Psychotherapy, University Hospital, LMU Munich, Munich, Germany; ⁴Centre for Discovery Brain Sciences, University of Edinburgh, Edinburgh, United Kingdom; ⁵Institute of Anatomy, University of Leipzig, Leipzig, Germany; ⁶Department of Clinical Neurophysiology, University Medical Center, Göttingen, Germany

Abstract Proteome and transcriptome analyses aim at comprehending the molecular profiles of the brain, its cell-types and subcellular compartments including myelin. Despite the relevance of the peripheral nervous system for normal sensory and motor capabilities, analogous approaches to peripheral nerves and peripheral myelin have fallen behind evolving technical standards. Here we assess the peripheral myelin proteome by gel-free, label-free mass-spectrometry for deep quantitative coverage. Integration with RNA-Sequencing-based developmental mRNA-abundance profiles and neuropathy disease genes illustrates the utility of this resource. Notably, the periaxin-deficient mouse model of the neuropathy Charcot-Marie-Tooth 4F displays a highly pathological myelin proteome profile, exemplified by the discovery of reduced levels of the monocarboxylate transporter MCT1/SLC16A1 as a novel facet of the neuropathology. This work provides the most comprehensive proteome resource thus far to approach development, function and pathology of peripheral myelin, and a straightforward, accurate and sensitive workflow to address myelin diversity in health and disease.

*For correspondence:
hauke@em.mpg.de

†These authors contributed
equally to this work

Competing interests: The
authors declare that no
competing interests exist.

Funding: See page 22

Received: 27 August 2019

Accepted: 19 February 2020

Published: 04 March 2020

Reviewing editor: Beth Stevens,
Boston Children's Hospital,
United States

© Copyright Siems et al. This
article is distributed under the
terms of the [Creative Commons
Attribution License](#), which
permits unrestricted use and
redistribution provided that the
original author and source are
credited.

Introduction

The ensheathment of axons with myelin enables rapid impulse propagation, a prerequisite for normal motor and sensory capabilities of vertebrates (Weil et al., 2018; Hartline and Colman, 2007). This is illustrated by demyelinating neuropathies of the Charcot-Marie-Tooth (CMT) spectrum, in which mutations affecting myelin genes as *MPZ*, *PMP22*, *GJB1* and *PRX* impair myelin integrity and reduce the velocity of nerve conduction in the peripheral nervous system (PNS) (Rossor et al., 2013). Developmentally, myelination by Schwann cells in peripheral nerves is regulated by axonal neuregulin-1 (Michailov et al., 2004; Taveggia et al., 2005) and the basal lamina (Chernousov et al., 2008; Petersen et al., 2015; Ghidinelli et al., 2017) that is molecularly linked to the abaxonal Schwann cell membrane via integrins and the dystroglycan complex (Sherman et al., 2001; Masaki et al., 2002; Nodari et al., 2008; Raasakka et al., 2019). In adulthood, the basal lamina continues to enclose all axon/myelin-units (Hess and Lansing, 1953), probably to maintain myelin. Beyond regulation by extracellular cues, myelination involves multiple proteins mediating radial sorting of axons out of Remak bundles, myelin membrane growth and layer compaction (Sherman and Brophy, 2005; Pereira et al., 2012; Grove and Brophy, 2014; Monk et al., 2015; Feltri et al., 2016). For example, the Ig-domain containing myelin protein zero

(MPZ; also termed P0) mediates adhesion between adjacent extracellular membrane surfaces in compact myelin (Giese *et al.*, 1992). At their intracellular surfaces, myelin membranes are compacted by the cytosolic domain of MPZ/P0 together with myelin basic protein (MBP; previously termed P1) (Martini *et al.*, 1995; Nawaz *et al.*, 2013). Not surprisingly, MPZ/P0 and MBP were early identified as the most abundant peripheral myelin proteins (Greenfield *et al.*, 1973; Brostoff *et al.*, 1975).

A system of cytoplasmic channels through the otherwise compacted myelin sheath remains non-compacted throughout life, that is the adaxonal myelin layer, paranodal loops, Schmidt-Lanterman incisures (SLI), and abaxonal longitudinal and transverse bands of cytoplasm termed bands of Cajal (Sherman and Brophy, 2005; Nave and Werner, 2014; Kleopa and Sargiannidou, 2015). Non-compacted myelin comprises cytoplasm, cytoskeletal elements, vesicles and lipid-modifying enzymes, and thus numerous proteins involved in maintaining the myelin sheath. The cytosolic channels probably also represent transport routes toward Schwann cell-dependent metabolic support of myelinated axons (Court *et al.*, 2004; Beirowski *et al.*, 2014; Domènech-Estévez *et al.*, 2015; Kim *et al.*, 2016; Gonçalves *et al.*, 2017; Stassart *et al.*, 2018).

Considering that Schwann cells constitute a major proportion of the cells in the PNS, oligonucleotide microarray analyses have been used for mRNA abundance profiling of total sciatic nerves (Nagarajan *et al.*, 2002; Le *et al.*, 2005). Indeed, these systematic approaches allowed the identification of novel myelin constituents including non-compact myelin-associated protein (NCMAP/MP11) (Ryu *et al.*, 2008). Notwithstanding that the number of known peripheral myelin proteins has grown in recent years, a comprehensive molecular inventory has been difficult to achieve because applications of systematic ('omics') approaches specifically to Schwann cells and peripheral myelin remained comparatively scarce, different from studies addressing oligodendrocytes and CNS myelin (Zhang *et al.*, 2014; Patzig *et al.*, 2016b; Sharma *et al.*, 2015; Thakurela *et al.*, 2016; Marques *et al.*, 2016; de Monasterio-Schrader *et al.*, 2012). One main reason may be that the available techniques were not sufficiently straightforward for general application. For example, the protein composition of peripheral myelin was previously assessed by proteome analysis (Patzig *et al.*, 2011). However, at that time the workflow of sample preparation and data acquisition (schematically depicted in Figure 1A) was very labor-intensive and required a substantial amount of input material; yet the depth of the resulting datasets remained limited. In particular, differential myelin proteome analysis by 2-dimensional fluorescence intensity gel electrophoresis (2D-DIGE) requires considerable hands-on-time and technical expertise (Patzig *et al.*, 2011; Kangas *et al.*, 2016). While this method is powerful for the separation of proteoforms (Kusch *et al.*, 2017), it typically suffers from under-representation of highly basic and transmembrane proteins. It thus allows comparing the abundance of only few myelin proteins rather than quantitatively covering the entire myelin proteome. Because of these limitations and an only modest sample-to-sample reproducibility, 2D-DIGE analysis of myelin, although unbiased, has not been commonly applied beyond specialized laboratories.

The aim of the present study was to establish a straightforward and readily applicable workflow to facilitate both comprehensive knowledge about the protein composition of peripheral myelin and systematic assessment of differences between two states, for example, pathological alterations in a neuropathy model. The major prerequisites were the biochemical purification of myelin, its solubilization with the detergent ASB-14 and the subsequent automated digestion with trypsin during filter-aided sample preparation (FASP). The tryptic peptides were fractionated by liquid chromatography and analyzed by mass spectrometry for gel-free, label-free quantitative proteome analysis. More specifically, we used nano-flow ultra-performance liquid chromatography (nanoUPLC) coupled to an electrospray-ionization quadrupole time-of-flight (ESI-QTOF) mass spectrometer with ion mobility option, providing an orthogonal dimension of peptide separation. The utilized data-independent acquisition (DIA) strategy relies on collecting data in an alternating low and elevated energy mode (MS^E); it enables simultaneous sequencing and quantification of all peptides entering the mass spectrometer without prior precursor selection, as reviewed in Neilson *et al.* (2011) and Distler *et al.* (2014a). With their high-duty cycle utilized for the acquisition of precursor ions, MS^E -type methods are ideally suited to reliably quantify proteins based on peptide intensities. Notably, these methods do not involve the use of spectral libraries in the identification of proteins, different from other DIA strategies. Instead, the achieved high-complexity fragmentation spectra are deconvoluted before submission to dedicated search engines for peptide and protein identification (Geromanos *et al.*,

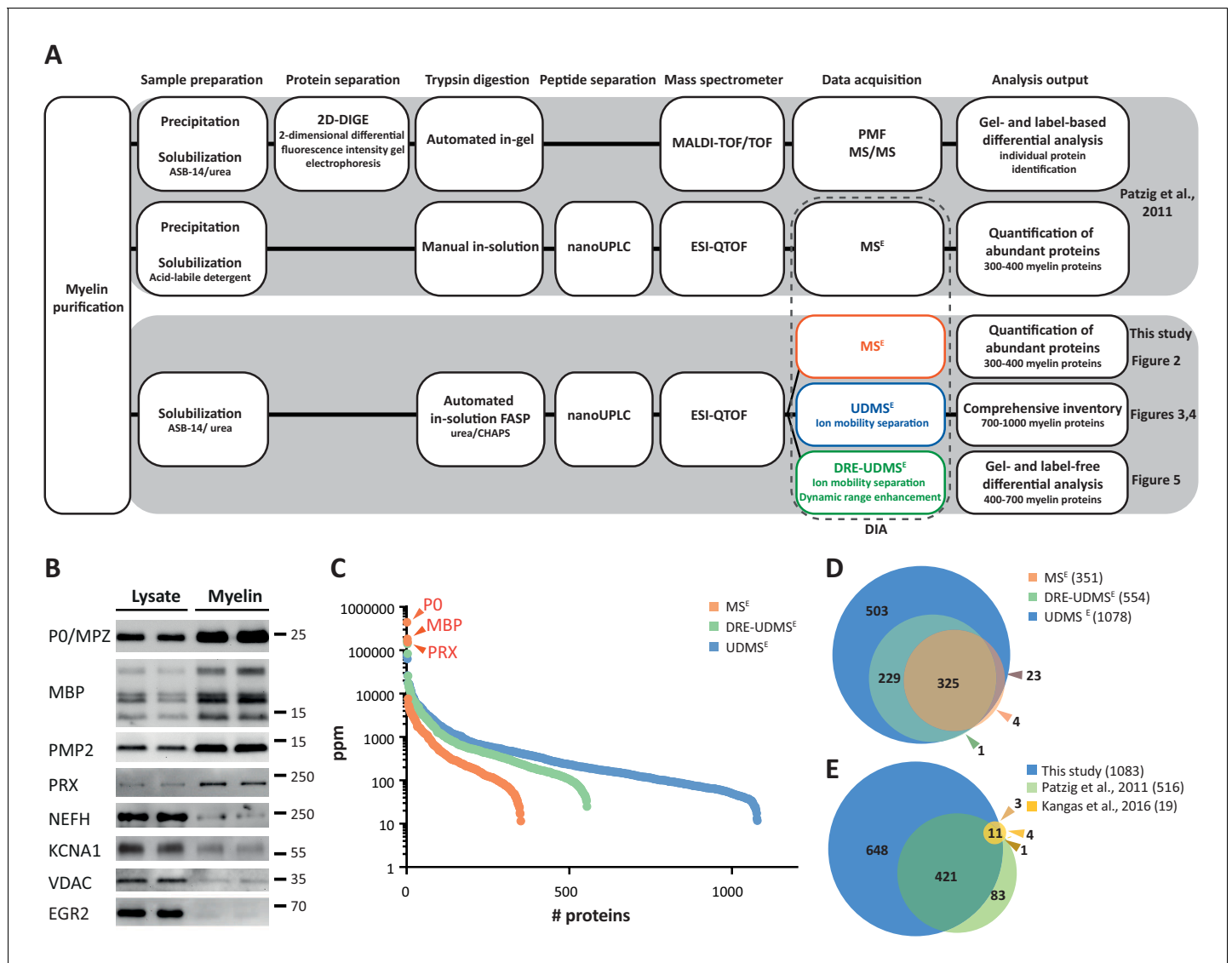


Figure 1. Proteome analysis of peripheral myelin. (A) Schematic illustration of a previous approach to the peripheral myelin proteome (*Patzig et al., 2011*) compared with the present workflow. Note that the current workflow allows largely automated sample processing and omits labor-intensive 2-dimensional differential gel-electrophoresis, thereby considerably reducing hands-on time. Nano LC-MS analysis by data-independent acquisition (DIA) using three different data acquisition modes provides efficient identification and quantification of abundant myelin proteins (MS^E; see *Figure 2*), a comprehensive inventory (UDMS^E; see *Figures 3–4*) and gel-free differential analysis of hundreds of distinct proteins (DRE-UDMS^E; see *Figure 5*). Samples were analyzed in three biological replicates. (B) Immunoblot of myelin biochemically enriched from sciatic nerves of wild-type mice at postnatal day 21 (P21). Equal amounts of corresponding nerve lysate were loaded to compare the abundance of marker proteins for compact myelin (MPZ/PO, MBP, PMP2), non-compact myelin (PRX), the Schwann cell nucleus (KROX20/EGR2), axons (NEFH, KCNA1) and mitochondria (VDAC). Blots show n = 2 biological replicates representative of n = 3 biological replicates. Note that myelin markers are enriched in purified myelin; other cellular markers are reduced. (C) Number and relative abundance of proteins identified in myelin purified from the sciatic nerves of wild-type mice using three different data acquisition modes (MS^E, UDMS^E, DRE-UDMS^E). Note that MS^E (orange) provides the best information about the relative abundance of high-abundant myelin proteins (dynamic range of more than four orders of magnitude) but identifies comparatively fewer proteins in purified myelin. UDMS^E (blue) identifies the largest number of proteins but provides only a lower dynamic range of about three orders of magnitude. DRE-UDMS^E (green) identifies an intermediate number of proteins with an intermediate dynamic range of about four orders of magnitude. Note that MS^E with very high dynamic range is required for the quantification of the exceptionally abundant myelin protein zero (MPZ/PO), myelin basic protein (MBP) and periaxin (PRX). ppm, parts per million. (D) Venn diagram comparing the number of proteins identified in PNS myelin by MS^E, UDMS^E and DRE-UDMS^E. Note the high overlap of identified proteins. (E) Venn diagram of the proteins identified in PNS myelin by UDMS^E in this study compared with those identified in two previous approaches (*Patzig et al., 2011*; *Kangas et al., 2016*).

The online version of this article includes the following source data and figure supplement(s) for figure 1:

Figure 1 continued on next page

Figure 1 continued

Source data 1. Label-free quantification of proteins in wild-type PNS myelin fractions by three different data acquisition modes Identification and quantification data of detected myelin-associated proteins.

Figure supplement 1. Clustered heatmap of Pearson's correlation coefficients for protein abundance comparing data acquisition modes.

2009; Li et al., 2009). In the MS^E mode, this deconvolution involves precursor-fragment ion alignment solely on the basis of chromatographic elution profiles. On top, drift times of ion mobility-separated precursors are used in the high-definition (HD)MS^E mode. An expansion of the latter, referred to as the ultra-definition (UD)MS^E mode, additionally implements drift time-dependent collision energy profiles for more effective precursor fragmentation (Distler et al., 2016; Distler et al., 2014b).

Indeed, compared to the previously used manual handling and in-gel digestion, the current workflow (schematically depicted in **Figure 1A**) is considerably less labor-intensive, and automated FASP increases sample-to-sample reproducibility. Moreover, differential analysis by quantitative mass spectrometry (MS) facilitates reproducible quantification of hundreds rather than a few distinct myelin proteins. Together, the present workflow increases the efficacy of assessing the peripheral myelin proteome while shifting the main workload from manual sample preparation and gel-separation to automated acquisition and processing of data. We propose that comprehending the expression profiles of all myelin proteins in the healthy PNS and in myelin-related disorders can contribute to advancing our understanding of the physiology and pathophysiology of peripheral nerves.

Results

Purification of peripheral myelin

We biochemically enriched myelin as a light-weight membrane fraction from pools of sciatic nerves dissected from mice at postnatal day 21 (P21) using an established protocol of discontinuous sucrose density gradient centrifugation (Patzig et al., 2011; Larocca and Norton, 2006), in which myelin membranes accumulate at the interface between 0.29 and 0.85 M sucrose. By immunoblotting, proteins specific for both compact (MPZ/P0, MBP, PMP2) and non-compact (PRX) myelin were substantially enriched in the myelin fraction compared to nerve lysates (**Figure 1B**). Conversely, axonal (NEFH, KCNA1) and mitochondrial (VDAC) proteins and a marker for the Schwann cell nucleus (KROX20/EGR2) were strongly reduced in purified myelin. Together, these results imply that biochemically purified peripheral myelin is suitable for systematic analysis of its protein composition.

Proteome analysis of peripheral myelin

It has long been difficult to accurately quantify the most abundant myelin proteins both in the CNS (PLP, MBP, CNP; Jahn et al., 2009) and the PNS (MPZ/P0, MBP, PRX; this work), probably owing to their exceptionally high relative abundance. For example, the major CNS myelin constituents PLP, MBP and CNP comprise 17, 8 and 4% of the total myelin protein, respectively (Jahn et al., 2009). We have recently provided proof of principle (Erwig et al., 2019a) that the mass spectrometric quantification of these high-abundant myelin proteins is accurate and precise when data are acquired in the MS^E data acquisition mode and proteins are quantified according to the TOP3 method, that is if their abundance values are obtained based on the proven correlation between the average intensity of the three peptides exhibiting the most intense mass spectrometry response and the absolute amount of their source protein (Silva et al., 2006; Ahrné et al., 2013). Using data acquisition by MS^E we confirmed that CNP constitutes about 4% of the total CNS myelin proteome and that the abundance of CNP in myelin from mice heterozygous for the *Cnp* gene (*Cnp*^{WT/null}) compared to wild-type mice is 50.7% (±0.4%), in agreement with the halved gene dosage and gel-based quantification by silver staining or immunoblotting (Erwig et al., 2019a).

When applying the MS^E mode to PNS myelin, we quantified 351 proteins with a false discovery rate (FDR) of <1% at peptide and protein level and an average sequence coverage of 35.5% (**Figure 1—source data 1**). While MS^E (labeled in orange in **Figure 1C**) indeed provided a dynamic range of more than four orders of magnitude and thus quantitatively covered the exceptionally abundant myelin proteins MPZ/P0, MBP and PRX, the number of quantified proteins appeared

limited when spectral complexity was deconvoluted solely on the basis of chromatographic elution profiles. Accordingly, by using the UDMS^E mode, which comprises ion mobility for additional peptide separation as well as drift time-specific collision energies for peptide fragmentation, proteome coverage was increased about three-fold (1078 proteins quantified; average sequence coverage 34.3%; **Figure 1—source data 1**). However, the dynamic range of UDMS^E (labeled in blue in **Figure 1C**) was found to be somewhat compressed compared to that of MS^E, which can be considered an expectable feature of traveling wave ion mobility devices (**Dodds and Baker, 2019**), where the analysis of pulsed ion packages leads to a temporal and spatial binning of peptides during ion mobility separation. Indeed, this manifests as a ceiling effect for the detection of exceptionally intense peptide signals, which results in an underestimation of the relative abundance of MPZ/P0, MBP and PRX by UDMS^E.

The complementary nature of the MS^E and UDMS^E data acquisition modes led us to conclude that a comprehensive analysis of the myelin proteome that facilitates both correct quantification of the most abundant proteins and deep quantitative coverage of the proteome would require analyzing the same set of samples with two different instrument settings for MS^E and UDMS^E, respectively. Considering that instrument time is a bottleneck for the routine differential proteome analysis of myelin from mutant mice, we aimed to combine the strengths of MS^E and UDMS^E into a single data acquisition mode. Based on a gene ontology enrichment analysis for cellular components of the 200 proteins of highest and lowest abundance from the UDMS^E dataset, we realized that the 'bottom' of the quantified proteome is probably largely unrelated to myelin but dominated by contaminants from other subcellular sources including mitochondria. We thus reasoned that for a myelin-directed data acquisition mode, proteome depth may be traded in for a gain in dynamic range and devised a novel method referred to as dynamic range enhancement (DRE)-UDMS^E, in which a deflection lens is used to cycle between full and reduced ion transmission during mass spectrometric scanning. Indeed, DRE-UDMS^E quantified an intermediate number of proteins in PNS myelin (554 proteins; average sequence coverage 30.6%; **Figure 1—source data 1**) while providing an intermediate dynamic range (labeled in green in **Figure 1C**). We thus consider DRE-UDMS^E as the data acquisition mode of choice most suitable for routine differential myelin proteome profiling (see below).

Overall, we found a high reproducibility between replicates and even among the different data acquisition modes as indicated by Pearson's correlation coefficients for protein abundance in the range of 0.765–0.997 (**Figure 1—figure supplement 1**). When comparing the proteins identified in PNS myelin using the three data acquisition modes, we found a very high overlap (**Figure 1D**). We also found a high overlap (**Figure 1E**) between the proteins identified in the present study by UDMS^E and those detected in previous proteomic approaches to PNS myelin (**Patzig et al., 2011; Kangas et al., 2016**), thus allowing a high level of confidence. Together, the three data acquisition modes exhibit distinct strengths in the efficient quantification of exceptionally abundant proteins (MS^E), establishing a comprehensive inventory (UDMS^E) and gel-free, label-free differential analysis of hundreds of distinct proteins (DRE-UDMS^E) in peripheral myelin (see **Figure 1A**). Yet, analyzing the same set of samples by different modes may not always be feasible in all routine applications when considering required instrument time.

Relative abundance of peripheral myelin proteins

Considering that MS^E provides the high dynamic range required for the quantification of the most abundant myelin proteins, we calculated the relative abundance of the 351 proteins identified in myelin by MS^E (**Figure 1—source data 1**). According to quantitative assessment of this dataset, the most abundant PNS myelin protein, myelin protein zero (MPZ/P0), constitutes 44% (+/- 4% relative standard deviation (RSD)) of the total myelin protein (**Figure 2**). Myelin basic protein (MBP), periaxin (PRX) and tetraspanin-29 (CD9) constitute 18% (+/- 1% RSD), 15% (+/- 1%) and 1% (+/- 0.2%) of the total myelin protein, respectively (**Figure 2**). For MPZ/P0 and MBP, our quantification by MS^E is in agreement with but specifies prior estimations upon gel-separation and protein labeling by Sudan-Black, Fast-Green or Coomassie-Blue, in which they were judged to constitute 45–70% and 2–26% of the total myelin protein, respectively (**Greenfield et al., 1973; Micko and Schlaepfer, 1978; Smith and Curtis, 1979; Whitaker, 1981**). However, gel-based estimates of the relative abundance of myelin proteins were not very precise with respect to many other proteins, including those of high molecular weight. Indeed, periaxin was identified as a constituent of peripheral myelin after the advent of gradient SDS-PAGE gels (**Gillespie et al., 1994**), which allowed improved migration of

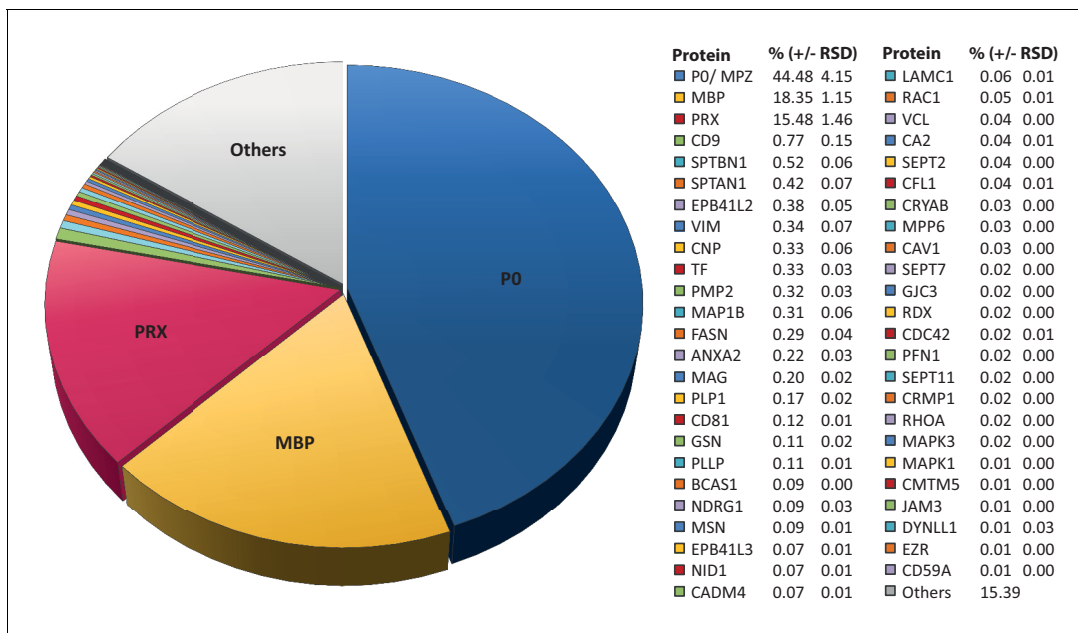


Figure 2. Relative abundance of peripheral myelin proteins. MS^E was used to identify and quantify proteins in myelin purified from the sciatic nerves of wild-type mice at P21; their relative abundance is given as percent with relative standard deviation (% +/- RSD). Note that known myelin proteins constitute >80% of the total myelin protein; proteins not previously associated with myelin constitute <20%. Mass spectrometric quantification based on 3 biological replicates per genotype with 4 technical replicates each (see [Figure 1—source data 1](#)).

large proteins into gels. The present MS^E-based quantification of myelin proteins also extends beyond and partially adjusts an earlier mass spectrometric approach ([Patzig et al., 2011](#)). Indeed, the current approach identified and quantified more myelin proteins, probably owing to improved protein solubilization during sample preparation and higher dynamic range of the used mass spectrometer. By MS^E, known myelin proteins ([Table 1](#)) collectively constitute over 85% of the total myelin protein ([Figure 2](#)) while proteins not yet associated with myelin account for the remaining 15% of the total myelin protein.

Comprehensive compendium and comparison to the transcriptome

To systematically elucidate the developmental abundance profiles of the transcripts that encode peripheral myelin proteins ([Figure 3](#)), we used our combined proteome inventory of peripheral myelin ([Figure 1—source data 1](#)) to filter mRNA abundance data of all genes expressed in sciatic nerves. By this strategy, [Figure 3](#) displays only those transcripts of which the protein product was identified in peripheral myelin rather than all transcripts in the nerve, thereby discriminating myelin-related mRNAs from other mRNAs such as those present in peripheral axons, fibroblasts, immune cells etc. In this assessment we additionally included PMP22 although it was not detected by MS as well as 45 proteins exclusively identified by LC-MS of myelin separated by SDS-PAGE ([Figure 1—source data 1](#)). For mRNA abundance profiles, we exploited a recently established RNA sequencing analysis (RNA-Seq; platform Illumina HiSeq 2000) of sciatic nerves dissected from wild type Sprague Dawley rats at embryonic day 21 (E21), P6, P18 and 6 months ([Fledrich et al., 2018](#)). RNA-Seq provides reliable information about the relative abundance of all significantly expressed genes and is thus not limited to those represented on the previously used oligonucleotide microarrays ([Patzig et al., 2011](#)). The raw data (accessible under GEO accession number GSE115930) were normalized ([Figure 3—source data 1](#)) and standardized. When comparing the proteome and transcriptome datasets, significant mRNA abundance was detected for all 1046 transcripts for which an unambiguous unique gene identifier was found ([Figure 3](#)). 126 transcripts displayed developmentally unchanged abundance levels, that is, abundance changes below a threshold of 10% coefficient of variation ([Figure 3B](#); [Figure 3—source data 1](#)).

Table 1. Known myelin proteins in the myelin proteome.

Proteins mass-spectrometrically identified in peripheral myelin are compiled according to availability of prior references as myelin proteins. Given are the official gene name, one selected reference, the number of transmembrane domains (TMD) and the mRNA abundance profile cluster (see **Figure 3**).

Protein name	Gene	Reference	TMD	Cluster
2-hydroxyacylsphingosine 1-beta-galactosyltransferase	<i>Ugt8</i>	<i>Bosio et al., 1996</i>	2	P6-up
Syntrophin α 1	<i>Snta1</i>	<i>Fuhrmann-Stroissnigg et al., 2012</i>	-	P18-up
Annexin A2	<i>Anxa2</i>	<i>Hayashi et al., 2007</i>	-	Descending
Band 4.1 protein B/4.1B	<i>Epb4113</i>	<i>Ivanovic et al., 2012</i>	-	Descending
Band 4.1 protein G/4.1G	<i>Epb4112</i>	<i>Ohno et al., 2006</i>	-	P6-up
Breast carcinoma-amplified sequence 1	<i>Bcas1</i>	<i>Ishimoto et al., 2017</i>	-	P6-up
Cadherin 1/E-Cadherin	<i>Cdh1</i>	<i>Fannon et al., 1995</i>	1	P18-up
Carbonic anhydrase 2	<i>Ca2</i>	<i>Cammer and Tansey, 1987</i>	-	Descending
Catenin α 1	<i>Ctnna1</i>	<i>Murata et al., 2006</i>	-	U-shaped
Catenin β 1	<i>Ctnnb1</i>	<i>Fannon et al., 1995</i>	-	Descending
Caveolin 1	<i>Cav1</i>	<i>Mikol et al., 2002</i>	1	P18-up
CD9, tetraspanin 29	<i>Cd9</i>	<i>Ishibashi et al., 2004</i>	4	P18-p
CD59A	<i>Cd59a</i>	<i>Funabashi et al., 1994</i>	1	P18-up
CD47, integrin-associated signal transducer	<i>Cd47</i>	<i>Gitik et al., 2011</i>	5	P6-up
CD81, tetraspanin 28	<i>Cd81</i>	<i>Ishibashi et al., 2004</i>	4	P18-up
CD82, tetraspanin 27	<i>Cd82</i>	<i>Chernousov et al., 2013</i>	4	P18-up
CD151, tetraspanin 24	<i>Cd151</i>	<i>Patzig et al., 2011</i>	4	P18-up
Cell adhesion molecule 4/NECL4	<i>Cadm4</i>	<i>Spiegel et al., 2007</i>	1	P6-up
Cell division control protein 42	<i>Cdc42</i>	<i>Benninger et al., 2007</i>	-	P6-up
Cell surface glycoprotein MUC18	<i>Mcam</i>	<i>Shih et al., 1998</i>	1	Descending
Ciliary neurotrophic factor	<i>Cntf</i>	<i>Rende et al., 1992</i>	-	Late-up
CKLF-like MARVEL TMD-containing 5	<i>Cmtm5</i>	<i>Patzig et al., 2011</i>	4	P6-up
Claudin-19	<i>Cldn19</i>	<i>Miyamoto et al., 2005</i>	4	P6-up
Cofilin 1	<i>Cfl1</i>	<i>Sparrow et al., 2012</i>	-	Descending
Crystallin α 2	<i>Cryab</i>	<i>D'Antonio et al., 2006</i>	-	P18-up
Cyclic nucleotide phosphodiesterase	<i>Cnp</i>	<i>Matthieu et al., 1980</i>	-	P6-up
Sarcoglycan δ	<i>Sgcd</i>	<i>Cai et al., 2007</i>	1	Late-up
Dihydropyrimidinase related protein 1	<i>Crmp1</i>	<i>D'Antonio et al., 2006</i>	-	Descending
Disks large homolog 1	<i>Dlg1</i>	<i>Cotter et al., 2010</i>	-	Descending
Dynein light chain 1	<i>Dynll1</i>	<i>Mylykoski et al., 2018</i>	-	P6-up
Dystroglycan	<i>Dag1</i>	<i>Yamada et al., 1994</i>	1	P6-up
Dystrophin/DP116	<i>Dmd</i>	<i>Cai et al., 2007</i>	-	P6-up
Dystrophin-related protein 2	<i>Drp2</i>	<i>Sherman et al., 2001</i>	-	P18-up
E3 ubiquitin-protein ligase NEDD4	<i>Nedd4</i>	<i>Liu et al., 2009</i>	-	Descending
Ezrin	<i>Ezr</i>	<i>Scherer et al., 2001</i>	-	P6-up
Fatty acid synthase	<i>Fasn</i>	<i>Salles et al., 2002</i>	-	P6-up
Flotillin 1	<i>Flot1</i>	<i>Lee et al., 2014</i>	-	P18-up
Gap junction β 1 protein/Cx32	<i>Gjb1</i>	<i>Li et al., 2002</i>	4	P18-up
Gap junction γ 3 protein/Cx29	<i>Gjc3</i>	<i>Li et al., 2002</i>	1	P6-up
Gelsolin	<i>Gsn</i>	<i>Gonçaves et al., 2010</i>	-	Late-up
Glycogen synthase kinase 3 β	<i>Gsk3b</i>	<i>Ogata et al., 2004</i>	-	P6-up

Table 1 continued on next page

Table 1 continued

Protein name	Gene	Reference	TMD	Cluster
Integrin $\alpha 6$	<i>Itga6</i>	Nodari et al., 2008	1	P6-up
Integrin αV	<i>Itgav</i>	Chernousov and Carey, 2003	1	Descending
Integrin $\beta 1$	<i>Itgb1</i>	Feltri et al., 2002	1	Descending
Integrin $\beta 4$	<i>Itgb4</i>	Quattrini et al., 1996	2	P18-up
Junctional adhesion molecule C	<i>Jam3</i>	Scheiermann et al., 2007	1	P18-up
Laminin $\alpha 2$	<i>Lama2</i>	Yang et al., 2005	-	P6-up
Laminin $\alpha 4$	<i>Lama4</i>	Yang et al., 2005	-	Descending
Laminin $\beta 1$	<i>Lamb1</i>	LeBeau et al., 1994	-	Descending
Laminin $\beta 2$	<i>Lamb2</i>	LeBeau et al., 1994	-	P18-up
Laminin $\gamma 1$	<i>Lamc1</i>	Chen and Strickland, 2003	-	Descending
Membrane Palmitoylated Protein 6	<i>Mpp6</i>	Saitoh et al., 2019	-	P6-up
Microtubule-associated protein 1A	<i>Map1a</i>	Fuhrmann-Stroissnigg et al., 2012	-	P18-up
Microtubule-associated protein 1B	<i>Map1b</i>	Fuhrmann-Stroissnigg et al., 2012	-	P6-up
Mitogen-activated protein kinase 1/ERK2	<i>Mapk1</i>	Mantuano et al., 2015	-	Descending
Mitogen-activated protein kinase 3/ERK1	<i>Mapk3</i>	Mantuano et al., 2015	-	P18-up
Moesin	<i>Msn</i>	Scherer et al., 2001	-	Unchanged
Monocarboxylate transporter 1	<i>Slc16a1</i>	Domènech-Estévez et al., 2015	11	P18-up
Myelin associated glycoprotein	<i>Mag</i>	Figlewicz et al., 1981	1	P6-up
Myelin basic protein	<i>Mbp</i>	Boggs, 2006	-	P6-up
Myelin protein 2	<i>Pmp2</i>	Trapp et al., 1984	-	P18-up
Myelin protein zero/P0	<i>Mpz</i>	Giese et al., 1992	1	P6-up
Myelin proteolipid protein	<i>Plp1</i>	Garbern et al., 1997	4	P6-up
Myotubularin-related protein 2	<i>Mtmr2</i>	Bolino et al., 2004	-	P6-up
Noncompact myelin-associated protein	<i>Ncmap</i>	Ryu et al., 2008	1	P18-up
NDRG1, N-myc downstream regulated	<i>Ndr1</i>	Berger et al., 2004	-	P18-uP
Neurofascin	<i>Nfasc</i>	Tait et al., 2000	2	P18-up
Nidogen 1	<i>Nid1</i>	Lee et al., 2007	-	Descending
P2X purinoceptor 7	<i>P2rx7</i>	Faroni et al., 2014	-	P6-up
Paxillin	<i>Pxn</i>	Fernandez-Valle et al., 2002	-	P6-up
Periaxin	<i>Prx</i>	Gillespie et al., 1994	-	P6-up
Plasmalipin	<i>Plip</i>	Bosse et al., 2003	4	P18-up
Profilin 1	<i>Pfn1</i>	Montani et al., 2014	-	Descending
Lin-7 homolog C	<i>Lin7c</i>	Saitoh et al., 2017	-	P6-up
Rac1	<i>Rac1</i>	Benninger et al., 2007	-	U-Shaped
Radixin	<i>Rdx</i>	Scherer et al., 2001	-	Descending
RhoA	<i>Rhoa</i>	Brancolini et al., 1999	-	U-Shaped
Septin 2	<i>Sept2</i>	Buser et al., 2009	-	Descending
Septin 7	<i>Sept7</i>	Buser et al., 2009	-	U-Shaped
Septin 8	<i>Sept8</i>	Patzig et al., 2011	-	P18-up
Septin 9	<i>Sept9</i>	Patzig et al., 2011	-	P6-up
Septin 11	<i>Sept11</i>	Buser et al., 2009	-	Descending
Sirtuin 2, NAD-dependent deacetylase	<i>Sirt2</i>	Werner et al., 2007	-	P18-up
Spectrin alpha chain, non-erythrocytic 1	<i>Sptan1</i>	Susuki et al., 2018	-	P18-up
Spectrin beta chain, non-erythrocytic 1	<i>Sptbn1</i>	Susuki et al., 2018	-	P18-up

Table 1 continued on next page

Table 1 continued

Protein name	Gene	Reference	TMD	Cluster
Tight junction protein ZO-1	<i>Tjp1</i>	<i>Poliak et al., 2002</i>	-	P6-up
Tight junction protein ZO-2	<i>Tjp2</i>	<i>Poliak et al., 2002</i>	-	P6-up
Transferrin	<i>Tf</i>	<i>Lin et al., 1990</i>	2	Late-up
Vimentin	<i>Vim</i>	<i>Triolo et al., 2012</i>	-	Unchanged
Vinculin	<i>Vcl</i>	<i>Beppu et al., 2015</i>	-	Descending

By fuzzy c-means clustering, those 920 transcripts that showed developmental abundance changes were grouped into 5 clusters (**Figure 3A**; **Figure 3—source data 1**). Among those, one cluster corresponds to an mRNA-abundance peak coinciding with an early phase of myelin biogenesis (cluster ‘P6-UP’), which includes the highest proportion of known myelin proteins (**Table 1**) such as MPZ/P0, MBP, PRX, cyclic nucleotide phosphodiesterase (CNP), fatty acid synthase (FASN), myelin-associated glycoprotein (MAG), proteolipid protein (PLP/DM20), cell adhesion molecule-4 (CADM4/NECL4), connexin-29 (GJC3), claudin-19 (CLDN19) and CKLF-like MARVEL-transmembrane domain containing protein-5 (CMTM5). However, many known myelin proteins clustered together according to their mRNA-abundance peak coinciding with a later phase of myelination (cluster ‘P18-UP’), including peripheral myelin protein 2 (PMP2), tetraspanin-29 (CD9), tetraspanin-28 (CD81), connexin-32 (GJB1), plasmalipin (PLLP), junctional adhesion molecule-3 (JAM3), CD59 and dystrophin-related protein-2 (DRP2). The proportion of known myelin proteins was lower in the clusters corresponding to mRNA-abundance peaks in adulthood (clusters ‘late-UP’, ‘U-shaped’). Yet, a considerable number of transcripts displayed abundance peaks at the embryonic time-point (cluster ‘Descending’), including carbonic anhydrase 2 (CA2), cofilin-1 (CFL1), tubulin beta-4 (TUBB4b) and band 4.1-protein B (EPB41L3). Generalized, the clusters were roughly similar when comparing previous oligonucleotide microarray analysis of mouse sciatic nerves (*Patzig et al., 2011*) and the RNA-Seq analysis of rat sciatic nerves (this study); yet, the latter provides information on a larger number of genes and with a higher level of confidence. Together, clustering of mRNA abundance profiles allows categorizing peripheral myelin proteins into developmentally co-regulated groups.

When systematically assessing the proteins identified in myelin by gene ontology (GO)-term analysis, the functional categories over-represented in the entire myelin proteome included cell adhesion, cytoskeleton and extracellular matrix (labeled in turquoise in **Figure 4**). When analyzing the clusters of developmentally co-expressed transcripts (from **Figure 3**), proteins associated with the lipid metabolism were particularly enriched in the P6-UP and P18-UP clusters, while those associated with the extracellular matrix (ECM) were over-represented in the U-shaped and Descending clusters (**Figure 4**). For comparison, known myelin proteins (**Table 1**) were over-represented in the P6-UP and P18-UP clusters (**Figure 4**). Together, our proteome dataset provides comprehensive in-depth coverage of the protein constituents of peripheral myelin purified from the sciatic nerves of wild type mice, and comparison to the transcriptome allows identifying developmentally co-regulated and functional groups of myelin proteins. Our data thus supply a solid resource for the molecular characterization of myelin and for discovering functionally relevant myelin proteins.

Neuropathy genes encoding myelin proteins

Heritable neuropathies can be caused by mutations affecting genes preferentially expressed in neurons, Schwann cells or both (*Rossor et al., 2013*; *Pareyson and Marchesi, 2009*; *Baets et al., 2014*; *Brennan et al., 2015*). To systematically assess which neuropathy-causing genes encode peripheral myelin proteins, we compared our myelin proteome dataset with a current overview about disease genes at the NIH National Library of Medicine at <https://ghr.nlm.nih.gov/condition/charcot-marie-tooth-disease#genes>. Indeed, 31 myelin proteins were identified to be encoded by a proven neuropathy gene (**Table 2**), a considerable increase compared to eight disease genes found in a similar previous approach (*Patzig et al., 2011*). Notably, this increase is owing to both the larger size of the current myelin proteome dataset (**Figure 1E**) and the recent discovery of numerous neuropathy genes by the widespread application of next generation sequencing.

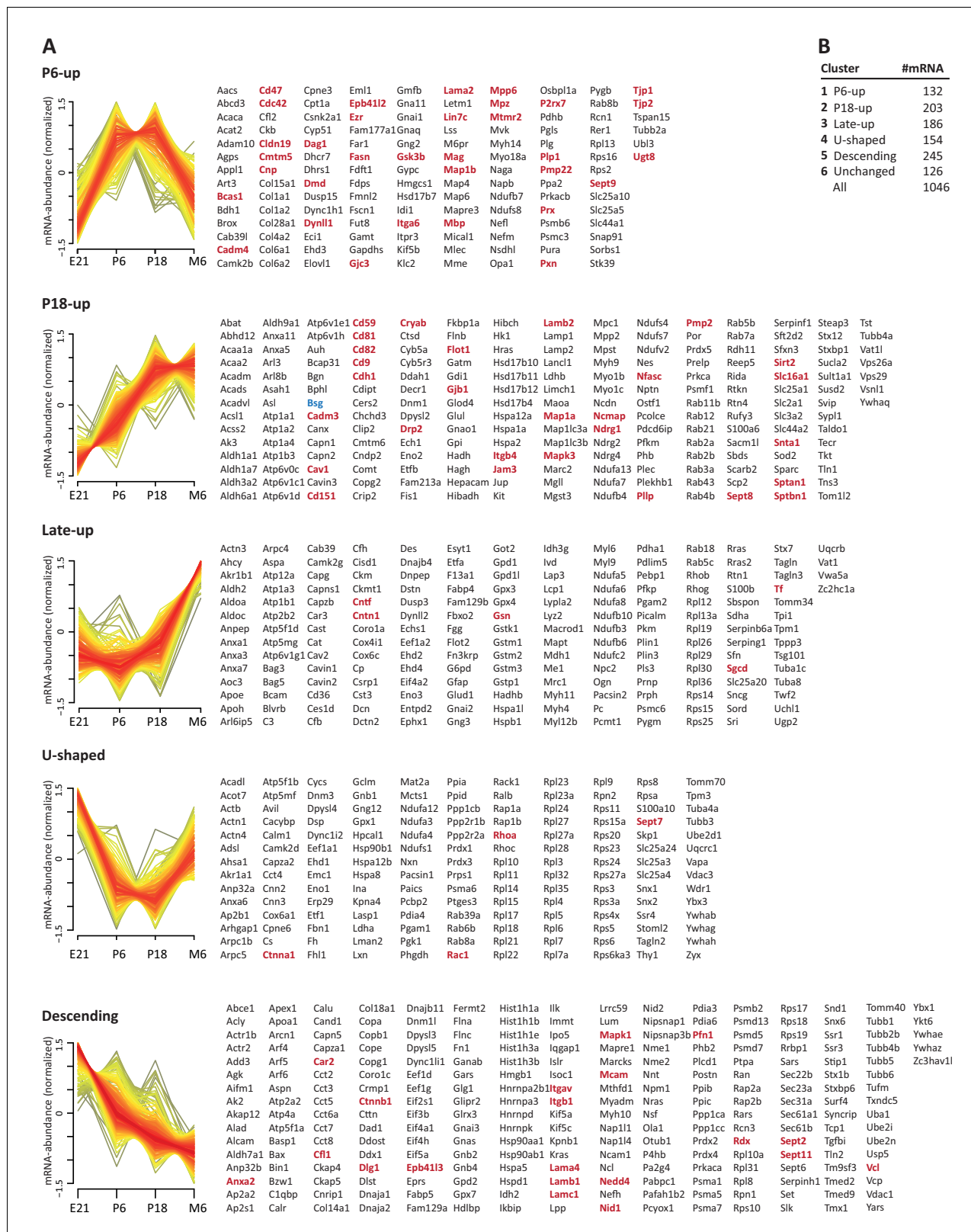


Figure 3. Developmental mRNA abundance profiles of myelin-associated genes. (A) K-means clustering was performed for the mRNA profiles of those 1046 proteins in our myelin proteome inventory for which significant mRNA expression was found by RNA-Seq in the sciatic nerve of rats dissected at ages E21, P6, P18 and 6 months (M6). Note that this filtering strategy allows to selectively display the developmental abundance profiles of those transcripts that encode myelin-associated proteins rather than of all transcripts present in the nerve. Standardized mRNA abundance profiles are shown *Figure 3 continued on next page*

Figure 3 continued

(n = 4 biological replicates per age). Known myelin genes are displayed in red. For comparison, *Pmp22* mRNA was included although the small tetraspan protein PMP22 was not mass spectrometrically identified due to its unfavorable distribution of tryptic cleavage sites. Normalized counts for all mRNAs including those displaying developmentally unchanged abundance are provided in **Figure 3—source data 1**. (B) Numbers of mRNAs per cluster.

The online version of this article includes the following source data for figure 3:

Source data 1. Normalized developmental mRNA abundance data → sheet 1: normalized values for all individual 4 biological replicates per age → sheet 2: normalized values for biological replicates averaged to give mean per age.

Pathological proteomic profile of peripheral myelin in a neuropathy model

The results presented thus far were based on analyzing myelin of healthy wild type mice; yet we also sought to establish a straightforward method to systematically assess myelin diversity, as exemplified by alterations in a pathological situation. As a model we chose mice carrying a homozygous deletion of the periaxin gene (*Prx*^{-/-}) (Court et al., 2004; Gillespie et al., 2000). Periaxin (PRX) is the third-most abundant peripheral myelin protein (Figure 2) and scaffolds the dystroglycan complex in Schwann cells. *Prx*^{-/-} mice represent an established model of Charcot-Marie-Tooth disease type 4F (Guilbot et al., 2001; Berger et al., 2006; Marchesi et al., 2010). Aiming to assess the myelin proteome, we purified myelin from pools of sciatic nerves dissected from *Prx*^{-/-} and control mice at P21. Upon SDS-PAGE separation and silver staining the band patterns appeared roughly similar (Figure 5A), with the most obvious exception of the absence of the high-molecular weight band constituted by periaxin in *Prx*^{-/-} myelin. Yet, several other bands also displayed genotype-dependent differences in intensity. As expected, PRX was also undetectable by MS^E in *Prx*^{-/-} myelin, in which

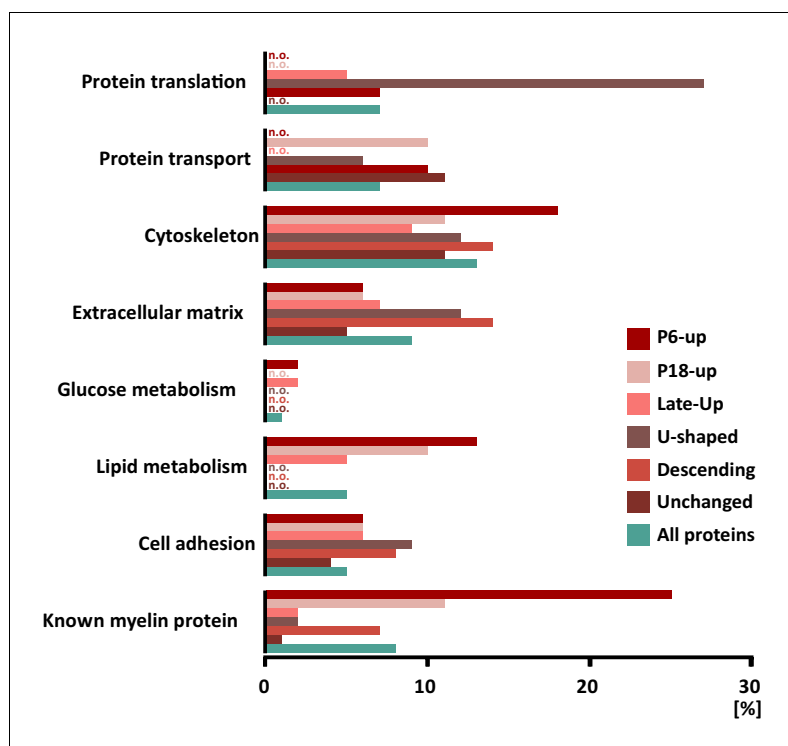


Figure 4. Categorization of annotated protein functions. All proteins identified in peripheral myelin by UDMS^E (turquoise) and the respective developmental expression clusters (Figure 3; shades of red) were analyzed for overrepresented functional annotations using gene ontology (GO) terms. The graph displays the percentage of proteins in each cluster that were annotated with a particular function. For comparison, known myelin proteins were annotated. n.o., not over-represented.

Table 2. Peripheral myelin proteins identified in PNS myelin involved in neuropathological diseases.

Proteins mass-spectrometrically identified in peripheral myelin were analyzed regarding the involvement of the ortholog human gene in neuropathological diseases. PMP22 was added, though it was not identified by MS analyses due to its unfavorable distribution of tryptic cleavage sites. CMT, Charcot-Marie-Tooth disease; DHMN, distal hereditary motor neuropathy; DI-CMTC, dominant intermediate CMTC; DFN, X-linked deafness; HMN, hereditary motor neuropathy; HSN, hereditary sensory and autonomic neuropathy; HNA, hereditary sensory and autonomic neuropathy; OMIM, Online Mendelian Inheritance in Man; PHARC, polyneuropathy, hearing loss, ataxia, retinitis pigmentosa and cataract; SCA, spinocerebellar ataxia; SPG, spastic paraplegia.

Protein name	Gene name	OMIM#	Gene locus	Neuropathy
Monoacylglycerol lipase ABHD12	<i>ABHD12</i>	613599	20p11.21	Pharc
Apoptosis-inducing factor 1	<i>AIFM1</i>	300169	Xq26.1	CMTX4, DFNX5
Na ⁺ /K ⁺ -transporting ATPase α 1	<i>ATP1A1</i>	182310	1p13.1	CMT2DD
Cytochrome c oxidase subunit 6A1	<i>COX6A1</i>	602072	12q24.31	CMTRID
Dystrophin-related protein 2	<i>DRP2</i>	300052	Xq22.1	CMTX
Dynactin subunit 1	<i>DCTN1</i>	601143	2p13.1	DHMN7B
Dynamain 2	<i>DNM2</i>	602378	19p13.2	CMT2M, CMTDIB
Cytoplasmic dynein 1 heavy chain 1	<i>DYNC1H1</i>	600112	14q32.31	CMT20, SMALED1
E3 SUMO-protein ligase	<i>EGR2</i>	129010	10q21.3	CMT1D, CMT3, CMT4E
Glycine-tRNA ligase	<i>GARS</i> (Gart)	600287	7p14.3	CMT2D, HMN5A
Gap junction β 1 protein/Cx32	<i>GJB1</i>	304040	Xq13.1	CMTX1
Guanine nucleotide-binding protein β 4	<i>GNB4</i>	610863	3q26.33	CMTDIF
Histidine triad nucleotide-binding protein 1	<i>HINT1</i>	601314	5q23.3	NMAN
Hexokinase 1	<i>HK1</i>	142600	10q22.1	CMT4G
Heat shock protein β 1	<i>HSPB1</i>	602195	7q11.23	CMT2F, DHMN2B
Kinesin heavy chain isoform 5A	<i>KIF5A</i>	602821	12q13.3	SPG10
Prelamin A/C	<i>LMNA</i>	150330	1q22	CMT2B1
Nephrilysin	<i>MME</i>	120520	3q25.2	CMT2T, SCA43
Myelin protein zero/P0	<i>MPZ</i>	159440	1q23.3	CHN2, CMT1B, CMT2I, CMT2J, CMT3, CMTDID, Roussy-Levy syndrome
Myotubularin-related protein 2	<i>MTMR2</i>	603557	11q21	CMT4B1
Alpha-N-acetylglucosaminidase	<i>NAGLU</i> (NAGA)	609701	17q21.2	CMT2V
NDRG1, N-myc downstream regulated	<i>NDRG1</i>	605262	8q24.22	CMT4D
Neurofilament heavy polypeptide	<i>NEFH</i>	162230	22q12.2	CMT2CC
Neurofilament light polypeptide	<i>NEFL</i>	162280	8p21.2	CMT2E, CMT1F, CMTDIG
Peripheral myelin protein 2	<i>PMP2</i>	170715	8q21.13	CMT1G
Peripheral myelin protein 22	<i>PMP22</i>	601907	17p12	CMT1A, CMT1E, CMT3, HNPP, Roussy-Levy syndrome
Ribose-phosphate pyrophosphokinase 1	<i>PRPS1</i>	311850	Xq22.3	Arts syndrome, CMTX5, DFNX1
Periaxin	<i>PRX</i>	605725	19q13.2	CMT4F, CMT3
Ras-related protein Rab 7a	<i>RAB7A</i>	602298	3q21.3	CMT2B
Septin 9	<i>SEPT9</i>	604061	17q25.3	HNA
Transitional ER-ATPase	<i>VCP</i>	601023	9p13.3	CMT2Y
Tryptophan-tRNA ligase, cytoplasmic	<i>WARS</i>	191050	14q32.32	HMN9
Tyrosine-tRNA ligase, cytoplasmic	<i>YARS</i>	603623	1p35.1	DI-CMTC

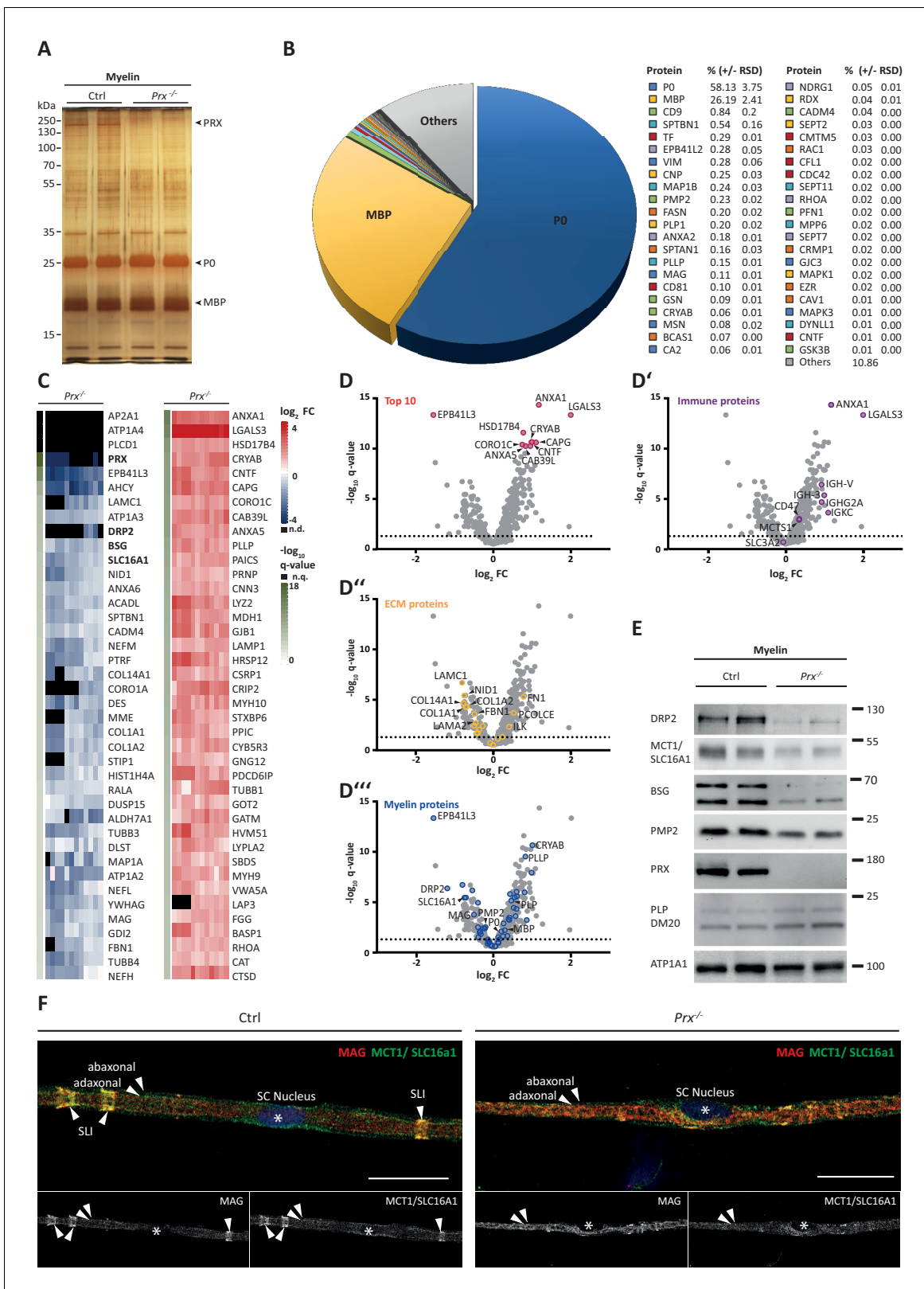


Figure 5. Molecular analysis of myelin in the *Prx*^{-/-} mouse model of CMT4F. (A) Myelin purified from sciatic nerves dissected from *Prx*^{-/-} and control mice at P21 was separated by SDS-PAGE (0.5 μg protein load) and proteins were visualized by silver staining. Bands constituted by the most abundant myelin proteins (MPZ/PO, MBP, PRX) are annotated. Note that no band constituted by PRX was detected in *Prx*^{-/-} myelin and that several other bands also display genotype-dependent differences in intensity. Gel shows n = 2 biological replicates representative of n = 3 biological replicates. (B) The Figure 5 continued on next page

Figure 5 continued

relative abundance of proteins in myelin purified from *Prx*^{-/-} sciatic nerves as quantified by MS^E is given as percent with relative standard deviation (% +/- RSD). Note the increased relative abundance of MPZ/P0 and MBP compared to wild-type myelin (see **Figure 2**) when PRX is lacking. Mass spectrometric quantification based on 3 biological replicates with 4 technical replicates each (see **Figure 5—source data 1**). (C,D) Differential proteome analysis by DRE-UDMS^E of myelin purified from *Prx*^{-/-} and wild-type mice. Mass spectrometric quantification based on 3 biological replicates per genotype with 4 technical replicates each (see **Figure 5—source data 2**). (C) Top 40 proteins of which the abundance is reduced (blue) or increased (red) in peripheral myelin purified from *Prx*^{-/-} compared to wild-type mice with the highest level of significance according to the $-\log_{10}$ transformed q-value (green). In the heatmaps, each horizontal line corresponds to the fold-change (FC) of a distinct protein compared to its average abundance in wild-type myelin plotted on a \log_2 color scale. Heatmaps display 12 replicates, that is 3 biological replicates per genotype with 4 technical replicates each. (D-D'') Volcano plots representing genotype-dependent quantitative myelin proteome analysis. Data points represent quantified proteins in *Prx*^{-/-} compared to wild-type myelin and are plotted as the \log_2 -transformed fold-change (FC) on the x-axis against the $-\log_{10}$ -transformed q-value on the y-axis. Stippled lines mark a $-\log_{10}$ -transformed q-value of 1.301, reflecting a q-value of 0.05 as significance threshold. Highlighted are the datapoints representing the Top 10 proteins displaying highest zdist values (Euclidean distance between the two points (0,0) and (x,y) with $x = \log_2(\text{FC})$ and $y = -\log_{10}(\text{q-value})$) (red circles in **D**), immune-related proteins (purple circles in **D'**), proteins of the extracellular matrix (ECM; yellow circles in **D''**) and known myelin proteins (blue circles in **D'''**). n.d., not detected; n.q., no q-value computable due to protein identification in one genotype only. Also see **Figure 5—figure supplement 1**. (E) Immunoblot of myelin purified from *Prx*^{-/-} and control sciatic nerves confirms the reduced abundance of DRP2, SLC16A1/MCT1, BSG and PMP2 in *Prx*^{-/-} myelin, as found by differential DRE-UDMS^E analysis (in **C,D**). PRX was detected as genotype control; PLP/DM20 and ATP1A1 serve as markers. Blot shows n = 2 biological replicates per genotype. (F) Teased fiber preparations of sciatic nerves dissected from *Prx*^{-/-} and control mice immunolabelled for MAG (red) and SLC16A1 (green). Note that SLC16A1 co-distributes with MAG in Schmidt-Lanterman incisures (SLI) in control but not in *Prx*^{-/-} nerves, in accordance with the reduced abundance of SLC16A1 in *Prx*^{-/-} myelin (**C–E**). Also note that, in *Prx*^{-/-} myelin, SLI were largely undetectable by MAG immunolabeling.

The online version of this article includes the following source data and figure supplement(s) for figure 5:

Source data 1. Label-free quantification of proteins in PNS myelin fractions from *Prx*^{-/-} mice by MS^E Identification and quantification data of detected myelin-associated proteins.

Source data 2. Label-free quantification of proteins in PNS myelin fractions from WT and *Prx*^{-/-} mice by DRE-UDMS^E Identification and quantification data of detected myelin-associated proteins by DRE-UDMS^E.

Figure supplement 1. Clustered heatmap of Pearson's correlation coefficients for protein abundance comparing genotypes.

most of the total myelin protein was constituted by MPZ/P0 and MBP (**Figure 5B**; **Figure 5—source data 1**).

Upon differential analysis by DRE-UDMS^E (**Figure 5—source data 2**), multiple proteins displayed genotype-dependent differences as visualized in a heatmap displaying those 40 proteins of which the abundance was reduced or increased with the highest statistical significance in *Prx*^{-/-} compared to control myelin (**Figure 5C**). For example, the abundance of the periaxin-associated dystrophin-related protein 2 (DRP2) was strongly reduced in *Prx*^{-/-} myelin, as previously shown by immunoblotting (**Sherman et al., 2001**). Notably, the abundance of multiple other proteins was also significantly reduced in *Prx*^{-/-} myelin, including the extracellular matrix protein laminin C1 (LAMC1; previously termed LAMB2), the laminin-associated protein nidogen (NID1), Ig-like cell adhesion molecules (CADM4, MAG), the desmosomal junction protein desmin (DES), cytoskeletal and cytoskeleton-associated proteins (EPB41L3, MAP1A, CORO1A, SPTBN1, various microtubular and intermediate filament monomers), the monocarboxylate transporter MCT1 (also termed SLC16A1) and the MCT1-associated (**Philp et al., 2003**) immunoglobulin superfamily protein basigin (BSG, also termed CD147). On the other hand, proteins displaying the strongest abundance increase in *Prx*^{-/-} myelin included immune-related proteins (LGALS3, LY2Z, CTSD), cytoskeletal and cytoskeleton-associated proteins (CAPG, CORO1C, CNN3, several myosin heavy chain subunits), peroxisomal enzymes (CAT, HSD17B4, MDH1) and known myelin proteins (PLLP/plasmolipin, CRYAB, GJB1/CX32). For comparison, the abundance of the marker proteolipid protein (PLP/DM20) (**Patzig et al., 2016a**) and the periaxin-associated integrin beta-4 (ITGB4) (**Raasakka et al., 2019**) in myelin was unaltered in *Prx*^{-/-} myelin. Together, differential proteome analysis finds considerably more proteins and protein groups to be altered in *Prx*^{-/-} myelin than previously known (**Figure 5C,D–D''**), probably reflecting the complex pathology observed in this model (**Court et al., 2004**; **Gillespie et al., 2000**).

The monocarboxylate transporter MCT1/SLC16A1 expressed by myelinating oligodendrocytes (**Lee et al., 2012**; **Fünfschilling et al., 2012**) and Schwann cells (**Domènech-Estévez et al., 2015**; **Morrison et al., 2015**) has been proposed to supply lactate or other glucose breakdown products to axons, in which they may serve as substrate for the mitochondrial production of ATP (**Morrison et al., 2013**; **Saab et al., 2013**; **Rinholm and Bergersen, 2014**). In this respect it was

striking to find the abundance of MCT1 significantly reduced in peripheral myelin when PRX is lacking (**Figure 5C**), a result that we were able to confirm by immunoblotting (**Figure 5E**) and immunolabeling of teased fiber preparations of sciatic nerves (**Figure 5F**). Notably, reduced expression of MCT1 in *Slc16a1*^{+/-} mice impairs axonal integrity at least in the CNS (**Lee et al., 2012; Jha et al., 2020**). The reduced abundance of MCT1 thus represents an interesting novel facet of the complex pathology in *Prx*^{-/-} mice. Considering that the integrity of peripheral axons may be impaired in *Prx*^{-/-} mice, we assessed their quadriceps nerves. Indeed, *Prx*^{-/-} mice displayed reduced axonal diameters, a progressively reduced total number of axons and a considerable number of myelin whorls lacking a visible axon (**Figure 6**), indicative of impaired axonal integrity (**Edgar et al., 2009**). Yet we note that molecular or neuropathological features other than the reduced abundance of MCT1 probably also contribute to the axonopathy in *Prx*^{-/-} mice.

Together, gel-free, label free proteome analysis provides a cost- and time-efficient method that provides an accurate, sensitive tool to gain systematic insight into the protein composition of healthy peripheral myelin and its alterations in pathological situations. Indeed, gel-free proteome analysis is particularly powerful and comprehensive compared to 2D-DIGE; the workflow presented here appears readily applicable to other neuropathy models, thereby promising discovery of relevant novel features of their neuropathology.

Discussion

We used gel-free, label-free quantitative mass spectrometry to assess the protein composition of myelin biochemically purified from the sciatic nerves of wild-type mice, thereby establishing a straightforward and readily applicable workflow to approach the peripheral myelin proteome. The key to comprehensiveness was to combine the strengths of three data acquisition modes, that is, MS^E for correct quantification of high-abundant proteins, UDMS^E for deep quantitative proteome coverage including low-abundant proteins and DRE-UDMS^E for differential analysis. We suggest that DRE-UDMS^E provides a good compromise between dynamic range, identification rate and instrument run time for routine differential myelin proteome profiling as a prerequisite for a molecular understanding of myelin (patho)biology. We have also integrated the resulting compendium with RNA-Seq-based mRNA abundance profiles in peripheral nerves and neuropathy disease loci. Beyond providing the largest peripheral myelin proteome dataset thus far, the workflow is appropriate to serve as starting point for assessing relevant variations of myelin protein composition, for example, in different nerves, ages, species and in pathological conditions. The identification of numerous pathological alterations of myelin protein composition in the *Prx*^{-/-} neuropathy model indicates that the method is well suited to assess such diversity.

Aiming to understand nervous system function at the molecular level, multiple 'omics'-scale projects assess the spatio-temporal expression profiles of all mRNAs and proteins in the CNS including oligodendrocytes and myelin (**Zhang et al., 2014; Patzig et al., 2016b; Sharma et al., 2015; Thakurela et al., 2016; Marques et al., 2016**). Yet, peripheral nerves are also essential for normal sensory and motor capabilities. Prior approaches to the molecular profiles of Schwann cells and PNS myelin thus far, however, were performed >8 years ago (**Nagarajan et al., 2002; Le et al., 2005; Ryu et al., 2008; Patzig et al., 2011; Verheijen et al., 2003; Buchstaller et al., 2004; D'Antonio et al., 2006**), and the techniques have considerably advanced since. For example, current gel-free, label-free mass spectrometry can simultaneously identify and quantify the vast majority of proteins in a sample, thereby providing comprehensive in depth-information. Moreover, RNA-Seq technology has overcome limitations of the previously used microarrays for characterizing mRNA abundance profiles with respect to the number of represented genes and the suitability of the oligonucleotide probes. The present compendium thus provides high confidence with respect to the identification of myelin proteins, their relative abundance and their developmental mRNA expression profiles. This view is supported by the finding that over 80% of the total myelin proteome is constituted by approximately 50 previously known myelin proteins. We believe that the majority of the other identified proteins represent low-abundant myelin-associated constituents in line with the high efficiency of biochemical myelin purification. Doubtless, however, the myelin proteome also comprises contaminants from other cellular sources, underscoring the need of independent validation for establishing newly identified constituents as true myelin proteins.

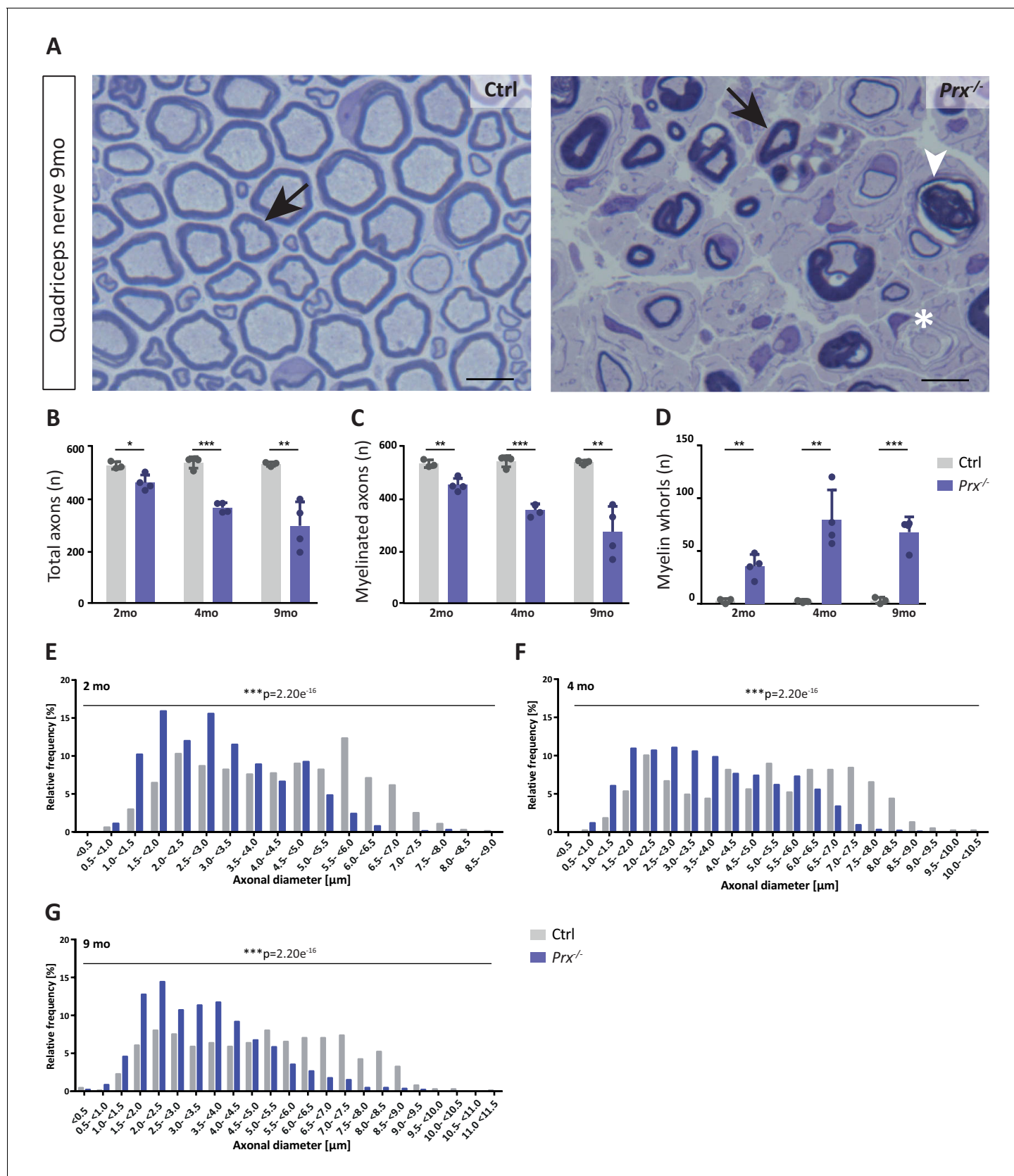


Figure 6. Progressive loss and reduced diameters of peripheral axons in *Prx*^{-/-} mice. (A–D) Genotype-dependent quantitative assessment of light micrographs of toluidine-stained semi-thin sectioned quadriceps nerves dissected at 2, 4 and 9 months of age reveals progressive loss of peripheral axons and reduced diameters of remaining axons. (E–G) Histograms showing the relative frequency of axonal diameters at 2, 4 and 9 months of age. Figure 6 continued on next page

Figure 6 continued

axons in *Prx*^{-/-} compared to control mice. (A) Representative micrographs. Arrows point at myelinated axons; asterisk denotes an unmyelinated axon; arrowhead points at a myelin whorl lacking a recognizable axon. Scale bars, 10 μ m. (B) Total number of axons per nerve that are not associated with a Remak bundle. (C) Total number of myelinated axons per nerve. (D) Total number per nerve of myelin whorls that lack a recognizable axon. Mean \pm SD, n = 3–4 mice per genotype and age; *p<0.05, **p<0.01, ***p<0.001 by Student's unpaired t-test. (E–G) Genotype-dependent assessment of myelinated axons shows a shift toward reduced axonal diameters in quadriceps nerves of *Prx*^{-/-} compared to control mice at 2 months (E), 4 months (F) and 9 months (G) of age. Data are presented as frequency distribution with 0.5 μ m bin width. ***, p<0.001 by two-sided Kolmogorow-Smirnow test. For precise p-values see methods section.

Do myelin proteins exist that escape identification by standard proteomic approaches? Indeed, some proteins display atypically distributed lysine and arginine residues, which represent the cleavage sites of the commonly used protease trypsin. The tryptic digest of these proteins leads to peptides that are not well suited for chromatographic separation and/or mass spectrometric detection/sequencing, as exemplified by the small hydrophobic tetraspan-transmembrane myelin proteins MAL (Schaeren-Wiemers et al., 2004) and PMP22 (Adlkofer et al., 1995). We can thus not exclude that additional proteins with atypical tryptic digest patterns exist in peripheral myelin, which would need to be addressed by the use of alternative proteases. Moreover, potent signaling molecules including erbB receptor tyrosine kinases (Riethmacher et al., 1997; Woldeyesus et al., 1999) and G-protein coupled receptors (GPRs) (Ackerman et al., 2018; Monk et al., 2011; Monk et al., 2009) display exceptionally low abundance. Such proteins may be identified when applying less stringent identification criteria, e.g., by requiring the sequencing of only one peptide per protein. However, lower stringency would also result in identifying false-positive proteins, which we wished to avoid for the purpose of the present compendium. We note that a truly comprehensive spatio-temporally resolved myelin proteome should preferentially also include systematic information about protein isoforms and post-translational modifications, which still poses technical challenges.

Mutations affecting the periaxin (PRX) gene in humans cause CMT type 4F (Guilbot et al., 2001; Kabzinska et al., 2006; Baránková et al., 2008; Tokunaga et al., 2012); the neuropathology resulting from mutations affecting periaxin has been mainly investigated in the *Prx*^{-/-} mouse model. Indeed, *Prx*^{-/-} mice display a progressive peripheral neuropathy including axon/myelin-units with abnormal myelin thickness, demyelination, tomaculae, onion bulbs, reduced nerve conduction velocity (Gillespie et al., 2000), reduced abundance and mislocalization of the periaxin-associated DRP2 (Sherman et al., 2001) and reduced internode length (Court et al., 2004). Absence of SLIs (Gillespie et al., 2000) and bands of Cajal (Court et al., 2004) imply that the non-compact myelin compartments are impaired when PRX is lacking. In the differential analysis of myelin purified from *Prx*^{-/-} and control mice we find that the previously reported reduced abundance of DRP2 (Sherman et al., 2001) represents one of the strongest molecular changes in the myelin proteome when PRX is lacking. Notably, the reported morphological changes in this neuropathy model (Sherman et al., 2001; Court et al., 2004; Gillespie et al., 2000) go along with alterations affecting the abundance of multiple other myelin-associated proteins, including junctional, cytoskeletal, extracellular matrix and immune-related proteins as well as lipid-modifying enzymes. Thus, the neuropathology in *Prx*^{-/-} mice at the molecular level is more complex than previously anticipated. It is striking that the abundance of the monocarboxylate transporter MCT1/SLC16A1 that may contribute to the metabolic supply of lactate from myelinating cells to axons (Beirowski et al., 2014; Domènech-Estévez et al., 2015; Kim et al., 2016; Gonçalves et al., 2017; Stassart et al., 2018) is strongly reduced in *Prx*^{-/-} myelin. Considering that MCT1 in Schwann cells mainly localizes to Schmidt Lanterman incisures (SLI) (Domènech-Estévez et al., 2015) and that SLI are largely absent from myelin when PRX is lacking (Gillespie et al., 2000), the reduced abundance of MCT1 in *Prx*^{-/-} myelin may be a consequence of the impaired myelin ultrastructure. Yet, considering that SLI are part of the cytosolic channels that may represent transport routes toward Schwann cell-dependent metabolic support of myelinated axons, the diminishment of MCT1 may contribute to reduced axonal diameters or axonal loss in *Prx*^{-/-} mice, probably in conjunction with other molecular or morphological defects. Together, the in depth-analysis of proteins altered in neuropathy models can contribute to an improved understanding of nerve pathophysiology.

Compared to a previous approach (Patzig et al., 2011), the number of proven neuropathy genes of which the encoded protein is mass spectrometrically identified in peripheral myelin has increased

four-fold from eight to 32 in the present study. This reflects both that the number of proteins identified in myelin has approximately doubled and that more neuropathy genes are known due to the common use of genome sequencing. We note that our compendium comprises not only myelin-associated proteins causing (when mutated) demyelinating CMT1 (e.g., MPZ/P0, NEFL, PMP2) or intermediate CMT4 (GDAP1, NDRG1, PRX) but also axonal CMT2 (RAB7, GARS, HSPB1). Yet, the expression of genes causative of CMT2 is not necessarily limited to neurons, as exemplified by the classical myelin protein MPZ/P0. Indeed, a subset of MPZ-mutations causes axonal CMT2I or CMT2J (Gallardo et al., 2009; Leal et al., 2014; Tokuda et al., 2015; Duan et al., 2016; Fabrizi et al., 2018), probably reflecting impaired axonal integrity as consequence of a mutation primarily affecting Schwann cells. We also note that the nuclear EGR2/KROX20 causative of demyelinating CMT1D has not been mass spectrometrically identified in myelin, reflecting that Schwann cell nuclei are efficiently removed during myelin purification.

While morphological analysis of peripheral nerves by light and electron microscopy is routine in numerous laboratories, systematic molecular analysis has been less straightforward. Using the sciatic nerve as a model, we show that systematic assessment of the myelin proteome and the total nerve transcriptome are suited to determine comprehensive molecular profiles in healthy nerves and in myelin-related disorders. Myelin proteome analysis can thus complement transcriptome analysis in assessing development, function and pathophysiology of peripheral nerves.

Materials and methods

Mouse models

Prx^{-/-} mice (Gillespie et al., 2000) were kept on c57Bl/6 background in the animal facility of the University of Edinburgh (United Kingdom). Genotyping was by PCR on genomic DNA using the forward primers 5'-CAGATTTGCT CTGCCCAAGT and 5'-CGCCTTCTAT CGCCTTCTTGAC in combination with reverse primer 5'-ATGCCCTCAC CCACTAACAG. The PCR yielded a 0.5 kb fragment for the wildtype allele and a 0.75 kb product for the mutant allele. The age of experimental animals is given in the figure legends. All animal work conformed to United Kingdom legislation (Scientific Procedures) Act 1986 and to the University of Edinburgh Ethical Review Committee policy; Home Office project license No. P0F4A25E9.

Myelin purification

A light-weight membrane fraction enriched for myelin was purified from sciatic nerves of mice by sucrose density centrifugation and osmotic shocks as described (Patzig et al., 2011; Erwig et al., 2019a). Myelin accumulates at the interface between 0.29 and 0.85 M sucrose. *Prx*^{-/-} and wild type control C57Bl/6 mice were sacrificed by cervical dislocation at postnatal day 21 (P21). For each genotype, myelin was purified as three biological replicates (n = 3); each biological replicate representing a pool of 20 sciatic nerves dissected from 10 mice. Protein concentration was determined using the DC Protein Assay Kit (Bio-Rad).

Filter-aided sample preparation for proteome analysis

Protein fractions corresponding to 10 µg myelin protein were dissolved and processed according to a filter-aided sample preparation (FASP) protocol essentially as previously described for synaptic protein fractions (Ambrozkiewicz et al., 2018) and as adapted to CNS myelin (Erwig et al., 2019a; Erwig et al., 2019b). Unless stated otherwise, all steps were automated on a liquid-handling workstation equipped with a vacuum manifold (Freedom EVO 150, Tecan) by using an adaptor device constructed in-house. Briefly, myelin protein samples were lysed and reduced in lysis buffer (7 M urea, 2 M thiourea, 10 mM DTT, 0.1 M Tris pH 8.5) containing 1% ASB-14 by shaking for 30 min at 37°C. Subsequently, the sample was diluted with ~10 volumes lysis buffer containing 2% CHAPS to reduce the ASB-14 concentration and loaded on centrifugal filter units (30 kDa MWCO, Merck Millipore). After removal of the detergents by washing twice with wash buffer (8 M urea, 10 mM DTT, 0.1 M Tris pH 8.5), proteins were alkylated with 50 mM iodoacetamide in 8 M urea, 0.1 M Tris pH 8.5 (20 min at RT), followed by two washes with wash buffer to remove excess reagent. Buffer was exchanged by washing three times with 50 mM ammonium bicarbonate (ABC) containing 10% acetonitrile. After three additional washes with 50 mM ABC/10% acetonitrile, which were performed by

centrifugation to ensure quantitative removal of liquids potentially remaining underneath the ultrafiltration membrane, proteins were digested overnight at 37°C with 400 ng trypsin in 40 µl of the same buffer. Tryptic peptides were recovered by centrifugation followed by two additional extraction steps with 40 µl of 50 mM ABC and 40 µl of 1% trifluoroacetic acid (TFA), respectively. Aliquots of the combined flow-throughs were spiked with 10 fmol/µl of yeast enolase-1 tryptic digest standard (Waters Corporation) for quantification purposes and directly subjected to analysis by liquid chromatography coupled to electrospray mass spectrometry (LC-MS). A pool of all samples was injected at least before and after any sample set to monitor stability of instrument performance.

Mass spectrometry

Nanoscale reversed-phase UPLC separation of tryptic peptides was performed with a nanoAcquity UPLC system equipped with a Symmetry C18 5 µm, 180 µm × 20 mm trap column and a HSS T3 C18 1.8 µm, 75 µm × 250 mm analytical column (Waters Corporation) maintained at 45°C. Injected peptides were trapped for 4 min at a flow rate of 8 µl/min 0.1% TFA and then separated over 120 min at a flow rate of 300 nl/min with a gradient comprising two linear steps of 3–35% mobile phase B in 105 min and 35–60% mobile phase B in 15 min, respectively. Mobile phase A was water containing 0.1% formic acid while mobile phase B was acetonitrile containing 0.1% formic acid. Mass spectrometric analysis of tryptic peptides was performed using a Synapt G2-S quadrupole time-of-flight mass spectrometer equipped with ion mobility option (Waters Corporation). Positive ions in the mass range m/z 50 to 2000 were acquired with a typical resolution of at least 20,000 FWHM (full width at half maximum) and data were lock mass corrected post-acquisition. UDMS^E and DRE-UDMS^E analyses were performed in the ion mobility-enhanced data-independent acquisition mode with drift time-specific collision energies as described in detail by *Distler et al. (2016)* and *Distler et al. (2014b)*. Specifically, for DRE-UDMS^E a deflection device (DRE lens) localized between the quadrupole and the ion mobility cell of the mass spectrometer was cycled between full (100% for 0.4 s) and reduced (5% for 0.4 s) ion transmission during one 0.8 s full scan. Continuum LC-MS data were processed for signal detection, peak picking, and isotope and charge state deconvolution using Waters ProteinLynx Global Server (PLGS) version 3.0.2 (47). For protein identification, a custom database was compiled by adding the sequence information for yeast enolase 1 and porcine trypsin to the UniProtKB/Swiss-Prot mouse proteome and by appending the reversed sequence of each entry to enable the determination of false discovery rate (FDR). Precursor and fragment ion mass tolerances were automatically determined by PLGS 3.0.2 and were typically below 5 ppm for precursor ions and below 10 ppm (root mean square) for fragment ions. Carbamidomethylation of cysteine was specified as fixed and oxidation of methionine as variable modification. One missed trypsin cleavage was allowed. Minimal ion matching requirements were two fragments per peptide, five fragments per protein, and one peptide per protein. The FDR for protein identification was set to 1% threshold.

Analysis of proteomic data

For each genotype (*Prx*^{-/-} and wild type control mice sacrificed at P21), biochemical fractions enriched for PNS myelin were analyzed as three biological replicates ($n = 3$ per condition); each biological replicate representing a pool of 20 sciatic nerves dissected from 10 mice. The samples were processed with replicate digestion and injection, resulting in four technical replicates per biological replicate and thus a total of 12 LC-MS runs per condition to be compared, essentially as previously reported for CNS myelin (*Patzig et al., 2016b*; *Erwig et al., 2019b*). The freely available software ISOQuant (www.isoquant.net) was used for post-identification analysis including retention time alignment, exact mass and retention time (EMRT) and ion mobility clustering, peak intensity normalization, isoform/homology filtering and calculation of absolute in-sample amounts for each detected protein (*Distler et al., 2016*; *Distler et al., 2014b*; *Kuharev et al., 2015*) according to the TOP3 quantification approach (*Silva et al., 2006*; *Ahrné et al., 2013*). Only peptides with a minimum length of seven amino acids that were identified with scores above or equal to 5.5 in at least two runs were considered. FDR for both peptides and proteins was set to 1% threshold and only proteins reported by at least two peptides (one of which unique) were quantified using the TOP3 method. The parts per million (ppm) abundance values (i.e. the relative amount (w/w) of each protein in respect to the sum over all detected proteins) were log₂-transformed and normalized by subtraction

of the median derived from all data points for the given protein. Significant changes in protein abundance were detected by moderated t-statistics essentially as described (*Ambrozkiewicz et al., 2018; Erwig et al. (2019b)*) across all technical replicates using an empirical Bayes approach and false discovery (FDR)-based correction for multiple comparisons (*Kammers et al., 2015*). For this purpose, the Bioconductor R packages 'limma' (*Ritchie et al., 2015*) and 'q-value' (*Storey, 2003*) were used in RStudio, an integrated development environment for the open source programming language R. Proteins identified as contaminants (e.g. components of blood or hair cells) were removed from the analysis. Proteins with ppm values below 100 which were not identified in one genotype were considered as just above detection level and also removed from the analysis. The relative abundance of a protein in myelin was accepted as altered if both statistically significant (q-value <0.05). Pie charts, heatmaps and volcano plots were prepared in Microsoft Excel 2013 and GraphPad Prism 7. Pearson's correlation coefficients derived from log₂-transformed ppm abundance values were clustered and visualized with the tool heatmap.2 contained in the R package gplots ([CRAN.R-project.org/package = gplots](https://CRAN.R-project.org/package=gplots)). Only pairwise complete observations were considered to reduce the influence of missing values on clustering behavior. The mass spectrometry proteomics data have been deposited to the ProteomeXchange Consortium (proteomecentral.proteomexchange.org) via the PRIDE partner repository (*Vizcaíno et al., 2016*) with the dataset identifier PXD015960.

Gel electrophoresis and silver staining of gels

Protein concentration was determined using the DC Protein Assay kit (BioRad). Samples were separated on a 12% SDS-PAGE for 1 hr at 200 V using the BioRad system, fixated overnight in 10% [v/v] acetic acid and 40% [v/v] ethanol and then washed in 30% ethanol (2 × 20 min) and ddH₂O (1 × 20 min). For sensitization, gels were incubated 1 min in 0.012% [v/v] Na₂S₂O₃ and subsequently washed with ddH₂O (3 × 20 s). For silver staining, gels were impregnated for 20 min in 0.2% [w/v] AgNO₃/0.04% formaldehyde, washed with ddH₂O (3 × 20 s) and developed in 3% [w/v] Na₂CO₃/0.02% [w/v] formaldehyde. The reaction was stopped by exchanging the solution with 5% [v/v] acetic acid.

Immunoblotting

Immunoblotting was performed as described by *Schardt et al. (2009)* and *de Monasterio-Schrader et al. (2013)*. Primary antibodies were specific for dystrophin-related-protein 2 (DRP2; Sigma; 1:1000), peripheral myelin protein 2 (PMP2; ProteinTech Group 12717-1-AP; 1:1000), proteolipid protein (PLP/DM20; A431; *Jung et al., 1996*; 1:5000), Monocarboxylate transporter 1 (MCT1/SLC16A1; *Stumpf et al., 2019*; 1:1000), periaxin (PRX; *Gillespie et al., 1994*; 1:1000), sodium/potassium-transporting ATPase subunit alpha-1 (ATP1A1; 1:2000; Abcam #13736-1-AP), myelin protein zero (MPZ/P0; *Archelos et al., 1993*; kind gift by J Archelos-Garcia; 1:10.000), voltage-dependent anion-selective channel protein (VDAC; Abcam #ab15895; 1:1000), basigin (BSG/CD147; Protein-Tech Group #ab64616; 1:1000), neurofilament H (NEFH/NF-H; Covance #SMI-32P; 1:1000), voltage-gated potassium channel subunit A member 1 (KCNA1; Neuromab #73-007; 1:1000), EGR2/KROX20 (*Darbas et al., 2004*; kind gift by D Meijer, Edinburgh; 1:1000) and myelin basic protein (MBP; 1:2000). To generate the latter antisera, rabbits were immunized (Pineda Antikörper Service, Berlin, Germany) with the KLH-coupled peptide CQDENPVVHFFK corresponding to amino acids 212–222 of mouse MBP isoform 1 (Swisprot/Uniprot-identifier P04370-1). Anti-MBP antisera were purified by affinity chromatography and extensively tested for specificity by immunoblot analysis of homogenate of brains dissected from wild-type mice compared to *Mbp^{shiverer/shiverer}* mice that lack expression of MBP. Appropriate secondary anti-mouse or -rabbit antibodies conjugated to HRP were from dianova. Immunoblots were developed using the Enhanced Chemiluminescence Detection kit (Western Lightning Plus, Perkin Elmer) and detected with the Intas ChemoCam system (INTAS Science Imaging Instruments GmbH, Göttingen, Germany).

Immunolabelling of teased fibers

Teased fibers were prepared as previously described by *Sherman et al. (2001)* and *Catenaccio and Court (2018)*. For each genotype, one male mouse was sacrificed by cervical dislocation at P17. Immunolabelling of teased fibers was performed as described by *Patzig et al. (2016b)*. Briefly, teased fibers were fixed for 5 min in 4% paraformaldehyde, permeabilized 5 min with ice-cold

methanol, washed in PBS (3 × 5 min) and blocked for 1 hr at 21°C in blocking buffer (10% horse serum, 0.25% Triton X-100, 1% bovine serum albumin in PBS). Primary antibodies were applied overnight at 4°C in incubation buffer (1.5% horse serum, 0.25% Triton X-100 in PBS). Samples were washed in PBS (3 × 5 min) and secondary antibodies were applied in incubation buffer (1 hr, RT). Samples were again washed in PBS (2 × 5 min), and 4',6-diamidino-2-phenylindole (DAPI; 1:50 000 in PBS) was applied for 10 min at RT. Samples were briefly washed 2x with ddH₂O and mounted using Aqua-Poly/Mount (Polysciences, Eppelheim, Germany). Antibodies were specific for myelin-associated glycoprotein (MAG clone 513; Chemicon MAB1567; 1:50) and MCT1/SLC16A1 (107). Secondary antibodies were donkey α -rabbit-Alexa488 (Invitrogen A21206; 1:1000) and donkey α -mouse-Alexa555 (Invitrogen A21202; 1:1000). Labeled teased fibers were imaged using the confocal microscope Leica SP5. The signal was collected with the objective HCX PL APO lambda blue 63.0. x1.20. DAPI staining was excited with 405 nm and collected between 417 nm - 480 nm. To excite the Alexa488 fluorophore an Argon laser with the excitation of 488 nm was used and the emission was set to 500 nm - 560 nm. Alexa555 was excited by using the DPSS561 laser at an excitation of 561 nm and the emission was set to 573 nm - 630 nm. To export and process the images LAS AF lite and Adobe Photoshop were used.

mRNA abundance profiles

Raw data were previously established (*Fledrich et al., 2018*) from the sciatic nerves of wild type Sprague Dawley rats at the indicated ages (E21, P6, P18; n = 4 per time point). Briefly, sciatic nerves were dissected, the epineurium was removed, total RNA was extracted with the RNeasy Kit (Qiagen), concentration and quality (ratio of absorption at 260/280 nm) of RNA samples were determined using the NanoDrop spectrophotometer (ThermoScientific), integrity of the extracted RNA was determined with the Agilent 2100 Bioanalyser (Agilent Technologies) and RNA-Seq was performed using the Illumina HiSeq2000 platform. RNA-Seq raw data are available under the GEO accession number GSE115930 (*Fledrich et al., 2018*). For the present analysis, the fastqfiles were mapped to *rattus norvegicus* rn6 using Tophat Aligner and then quantified based on the Ensemble Transcripts release v96. The raw read counts were then normalized using the R package DESeq2. The normalized gene expression data was then standardized to a mean of zero and a standard deviation of one, therefore genes with similar changes in expression are close in the euclidian space. Clustering was performed on the standardized data using the R package mfuzz. Transcripts displaying abundance differences of less than 10% coefficient of variation were considered developmentally unchanged.

Venn diagrams

Area-proportional Venn diagrams were prepared using BioVenn (*Hulsen et al., 2008*) at www.bio-venn.nl/.

GO-term

For functional categorization of the myelin proteome the associated gene ontology terms were systematically analyzed on the mRNA abundance cluster using the Database for Annotation, Visualization and Integrated Discovery (DAVID; <https://david.ncifcrf.gov>). For comparison known myelin proteins according to literature were added.

Histological analysis

Prx^{-/-} and control mice were perfused at the indicated ages intravascularly with fixative solution (2.5% glutaraldehyde, 4% paraformaldehyde, 0.1 M sodium cacodylate buffer, pH 7.4). Quadriceps nerves were removed, fixed for 2 hr at room temperature, followed by 18 hr at 4°C in the same fixative, postfixed in OsO₄, dehydrated a graded series of ethanol, followed by propylene oxide and embedded in Araldite. All axons not associated with a Remak bundle were counted and categorized as myelinated or non-myelinated. All myelin profiles lacking a recognizable axon were counted. The total number of axons were counted on micrographs of toluidine blue stained Araldite sections (0.5 μ m) of quadriceps nerves. Precise p-values for the quantitative comparison between Ctrl and *Prx*^{-/-} mice were: Total number of axons (*Figure 6B*; Student's unpaired t-test): 2 mo p=0.01734; 4 mo p=2.1E-05; 9 mo p=0.007625; Number of myelinated axons (*Figure 6C*; Student's unpaired t-test): 2

mo $p=0.00444$; 4 mo $p=2.12E-05$; 9 mo $p=0.005766$; Number of empty myelin profiles (**Figure 6D**; Student's unpaired t-test): 2 mo $p=0.004445$; 4 mo $p=0.001461$; 9 mo $p=0.000695$; Axonal diameters (**Figure 6E–G**; two-sided Kolmogorow-Smirnow test): 2 mo $p=2.20E-16$; 4 mo $p=2.20E-16$; 9 mo $p=2.20E-16$.

Acknowledgements

We thank J Archelos-Garcia and D Meijer for antibodies, T Buscham and J Edgar for discussions, L Piepkorn for support in data analysis, K-A Nave for support made possible by a European Research Council Advanced Grant ('MyeliNano' to K-AN) and the International Max Planck Research School for Genome Science (IMPRS-GS) for supporting SBS.

Additional information

Funding

Funder	Grant reference number	Author
Deutsche Forschungsgemeinschaft	WE 2720/2-2	Hauke B. Werner
Deutsche Forschungsgemeinschaft	WE 2720/4-1	Hauke B. Werner
Deutsche Forschungsgemeinschaft	WE 2720/5-1	Hauke B. Werner
Deutsche Forschungsgemeinschaft	RO 4076/3-2	Moritz J. Rossner
Wellcome	0842424	Peter Brophy

The funders had no role in study design, data collection and interpretation, or the decision to submit the work for publication.

Author contributions

Sophie B Siems, Performed all experiments not specified otherwise, conducted statistical analysis, contributed to analysis and interpretation of data; Olaf Jahn, Performed proteome analysis, contributed to analysis and interpretation of data and writing the article; Maria A Eichel, Performed teased fiber labeling and microscopy; Nirmal Kannaiyan, Performed bioinformatic analysis of RNA-Seq data; Lai Man N Wu, Diane L Sherman, Performed histological analysis; Kathrin Kusch, Provided unpublished reagents; Dörte Hesse, Contributed to proteome analysis; Ramona B Jung, Performed biochemical purification of myelin; Robert Fledrich, Michael W Sereda, Provided an unpublished RNA-Seq dataset; Moritz J Rossner, Supervised bioinformatic analysis of RNA-Seq data; Peter J Brophy, Supervised histological analysis; Hauke B Werner, Conceived, designed and directed the study, analyzed and interpreted data and wrote the article

Author ORCIDs

Olaf Jahn  <https://orcid.org/0000-0002-3397-8924>

Kathrin Kusch  <https://orcid.org/0000-0002-5079-502X>

Hauke B Werner  <https://orcid.org/0000-0002-7710-5738>

Ethics

Animal experimentation: All animal work conformed to United Kingdom legislation (Scientific Procedures) Act 1986 and to the University of Edinburgh Ethical Review Committee policy; Home Office project license No. P0F4A25E9.

Decision letter and Author response

Decision letter <https://doi.org/10.7554/eLife.51406.sa1>

Author response <https://doi.org/10.7554/eLife.51406.sa2>

Additional files

Supplementary files

- Transparent reporting form

Data availability

All data generated or analysed during this study are included in the manuscript and supporting files. This includes the mass spectrometry proteomics data. Source data files have been provided for Figures 1, 3 and 5. Additional to being provided in the source data files, mass spectrometry proteomics data have been deposited to the PRIDE/ProteomeXchange Consortium with dataset identifier PXD015960.

The following dataset was generated:

Author(s)	Year	Dataset title	Dataset URL	Database and Identifier
Olaf Jahn	2020	Proteome profile of peripheral myelin in healthy mice and in a neuropathy model	https://www.ebi.ac.uk/pride/archive/projects/PXD015960	PRIDE, PXD015960

References

- Ackerman SD, Luo R, Poitelon Y, Mogha A, Harty BL, D’Rozario M, Sanchez NE, Lakkaraju AKK, Gamble P, Li J, Qu J, MacEwan MR, Ray WZ, Aguzzi A, Feltri ML, Piao X, Monk KR. 2018. GPR56/ADGRG1 regulates development and maintenance of peripheral myelin. *Journal of Experimental Medicine* **215**:941–961. DOI: <https://doi.org/10.1084/jem.20161714>, PMID: 29367382
- Adlkofer K, Martini R, Aguzzi A, Zielasek J, Toyka KV, Suter U. 1995. Hypermyelination and demyelinating peripheral neuropathy in Pmp22-deficient mice. *Nature Genetics* **11**:274–280. DOI: <https://doi.org/10.1038/ng1195-274>, PMID: 7581450
- Ahrné E, Molzahn L, Glatter T, Schmidt A. 2013. Critical assessment of proteome-wide label-free absolute abundance estimation strategies. *Proteomics* **13**:2567–2578. DOI: <https://doi.org/10.1002/pmic.201300135>
- Ambrozkiwicz MC, Schwark M, Kishimoto-Suga M, Borisova E, Hori K, Salazar-Lázaro A, Rusanova A, Altas B, Piepkorn L, Bessa P, Schaub T, Zhang X, Rabe T, Ripamonti S, Rosário M, Akiyama H, Jahn O, Kobayashi T, Hoshino M, Tarabykin V, et al. 2018. Polarity acquisition in cortical neurons is driven by synergistic action of Sox9-Regulated Wwp1 and Wwp2 E3 ubiquitin ligases and intronic miR-140. *Neuron* **100**:1097–1115. DOI: <https://doi.org/10.1016/j.neuron.2018.10.008>, PMID: 30392800
- Archelos JJ, Roggenbuck K, Schneider-Schaulies J, Lington C, Toyka KV, Hartung HP. 1993. Production and characterization of monoclonal antibodies to the extracellular domain of P0. *Journal of Neuroscience Research* **35**:46–53. DOI: <https://doi.org/10.1002/jnr.490350107>, PMID: 7685397
- Baets J, De Jonghe P, Timmerman V. 2014. Recent advances in Charcot-Marie-Tooth disease. *Current Opinion in Neurology* **27**:532–540. DOI: <https://doi.org/10.1097/WCO.0000000000000131>, PMID: 25110935
- Baránková L, Sisková D, Hühne K, Vyhnálková E, Sakmaryová I, Bojar M, Rautenstrauss B, Seeman P. 2008. A 71-nucleotide deletion in the periaxin gene in a Romani patient with early-onset slowly progressive demyelinating CMT. *European Journal of Neurology* **15**:548–551. DOI: <https://doi.org/10.1111/j.1468-1331.2008.02104.x>, PMID: 18410371
- Beirowski B, Babetto E, Golden JP, Chen YJ, Yang K, Gross RW, Patti GJ, Milbrandt J. 2014. Metabolic regulator LKB1 is crucial for Schwann cell-mediated axon maintenance. *Nature Neuroscience* **17**:1351–1361. DOI: <https://doi.org/10.1038/nn.3809>, PMID: 25195104
- Benninger Y, Thurnherr T, Pereira JA, Krause S, Wu X, Chrostek-Grashoff A, Herzog D, Nave KA, Franklin RJ, Meijer D, Brakebusch C, Suter U, Relvas JB. 2007. Essential and distinct roles for cdc42 and rac1 in the regulation of Schwann cell biology during peripheral nervous system development. *The Journal of Cell Biology* **177**:1051–1061. DOI: <https://doi.org/10.1083/jcb.200610108>, PMID: 17576798
- Beppu M, Sawai S, Satoh M, Mori M, Kazami T, Misawa S, Shibuya K, Ishibashi M, Sogawa K, Kado S, Kodera Y, Nomura F, Kuwabara S. 2015. Autoantibodies against vinculin in patients with chronic inflammatory demyelinating polyneuropathy. *Journal of Neuroimmunology* **287**:9–15. DOI: <https://doi.org/10.1016/j.jneuroim.2015.07.012>, PMID: 26439954
- Berger P, Sirkowski EE, Scherer SS, Suter U. 2004. Expression analysis of the N-Myc downstream-regulated gene 1 indicates that myelinating Schwann cells are the primary disease target in hereditary motor and sensory neuropathy-Lom. *Neurobiology of Disease* **17**:290–299. DOI: <https://doi.org/10.1016/j.nbd.2004.07.014>, PMID: 15474366
- Berger P, Niemann A, Suter U. 2006. Schwann cells and the pathogenesis of inherited motor and sensory neuropathies (Charcot-Marie-Tooth disease). *Glia* **54**:243–257. DOI: <https://doi.org/10.1002/glia.20386>, PMID: 16856148

- Boggs JM.** 2006. Myelin basic protein: a multifunctional protein. *Cellular and Molecular Life Sciences* **63**:1945–1961. DOI: <https://doi.org/10.1007/s00018-006-6094-7>, PMID: 16794783
- Bolino A, Bolis A, Previtali SC, Dina G, Bussini S, Dati G, Amadio S, Del Carro U, Mruk DD, Feltri ML, Cheng CY, Quattrini A, Wrabetz L.** 2004. Disruption of Mtmr2 produces CMT4B1-like neuropathy with myelin outfolding and impaired spermatogenesis. *The Journal of Cell Biology* **167**:711–721. DOI: <https://doi.org/10.1083/jcb.200407010>, PMID: 15557122
- Bosio A, Binczek E, Stoffel W.** 1996. Functional breakdown of the lipid bilayer of the myelin membrane in central and peripheral nervous system by disrupted galactocerebroside synthesis. *PNAS* **93**:13280–13285. DOI: <https://doi.org/10.1073/pnas.93.23.13280>, PMID: 8917582
- Bosse F, Hasse B, Pippirs U, Greiner-Petter R, Müller HW.** 2003. Proteolipid plasmalogen: localization in polarized cells, regulated expression and lipid raft association in CNS and PNS myelin. *Journal of Neurochemistry* **86**: 508–518. DOI: <https://doi.org/10.1046/j.1471-4159.2003.01870.x>, PMID: 12871592
- Brancolini C, Marzinotto S, Edomi P, Agostoni E, Fiorentini C, Müller HW, Schneider C.** 1999. Rho-dependent regulation of cell spreading by the tetraspan membrane protein Gas3/PMP22. *Molecular Biology of the Cell* **10**:2441–2459. DOI: <https://doi.org/10.1091/mbc.10.7.2441>, PMID: 10397775
- Brennan KM, Bai Y, Shy ME.** 2015. Demyelinating CMT—what’s known, what’s new and what’s in store? *Neuroscience Letters* **596**:14–26. DOI: <https://doi.org/10.1016/j.neulet.2015.01.059>
- Brostoff SW, Karkhanis YD, Carlo DJ, Reuter W, Eylar EH.** 1975. Isolation and partial characterization of the major proteins of rabbit sciatic nerve myelin. *Brain Research* **86**:449–458. DOI: [https://doi.org/10.1016/0006-8993\(75\)90895-1](https://doi.org/10.1016/0006-8993(75)90895-1)
- Buchstaller J, Sommer L, Bodmer M, Hoffmann R, Suter U, Mantei N.** 2004. Efficient isolation and gene expression profiling of small numbers of neural crest stem cells and developing Schwann cells. *Journal of Neuroscience* **24**:2357–2365. DOI: <https://doi.org/10.1523/JNEUROSCI.4083-03.2004>, PMID: 15014110
- Buser AM, Erne B, Werner HB, Nave KA, Schaeren-Wiemers N.** 2009. The septin cytoskeleton in myelinating glia. *Molecular and Cellular Neuroscience* **40**:156–166. DOI: <https://doi.org/10.1016/j.mcn.2008.10.002>, PMID: 19026747
- Cai H, Erdman RA, Zweier L, Chen J, Shaw JH, Baylor KA, Stecker MM, Carey DJ, Chan YM.** 2007. The sarcoglycan complex in Schwann cells and its role in myelin stability. *Experimental Neurology* **205**:257–269. DOI: <https://doi.org/10.1016/j.expneurol.2007.02.015>, PMID: 17397833
- Cammer W, Tansey FA.** 1987. Immunocytochemical localization of carbonic anhydrase in myelinated fibers in peripheral nerves of rat and mouse. *Journal of Histochemistry & Cytochemistry* **35**:865–870. DOI: <https://doi.org/10.1177/35.8.3110266>, PMID: 3110266
- Catenaccio A, Court FA.** 2018. Teased fiber preparation of myelinated nerve fibers from peripheral nerves for vital dye staining and immunofluorescence analysis. *Methods in Molecular Biology* **1739**:329–337. DOI: https://doi.org/10.1007/978-1-4939-7649-2_21, PMID: 29546717
- Chen ZL, Strickland S.** 2003. Laminin gamma1 is critical for Schwann cell differentiation, axon myelination, and regeneration in the peripheral nerve. *Journal of Cell Biology* **163**:889–899. DOI: <https://doi.org/10.1083/jcb.200307068>, PMID: 14638863
- Chernousov MA, Yu WM, Chen ZL, Carey DJ, Strickland S.** 2008. Regulation of Schwann cell function by the extracellular matrix. *Glia* **56**:1498–1507. DOI: <https://doi.org/10.1002/glia.20740>, PMID: 18803319
- Chernousov MA, Stahl RC, Carey DJ.** 2013. Tetraspanins are involved in Schwann cell-axon interaction. *Journal of Neuroscience Research* **91**:1419–1428. DOI: <https://doi.org/10.1002/jnr.23272>, PMID: 24038174
- Chernousov MA, Carey DJ.** 2003. alphaVbeta8 integrin is a Schwann cell receptor for fibrin. *Experimental Cell Research* **291**:514–524. DOI: [https://doi.org/10.1016/S0014-4827\(03\)00409-9](https://doi.org/10.1016/S0014-4827(03)00409-9), PMID: 14644171
- Cotter L, Ozçelik M, Jacob C, Pereira JA, Locher V, Baumann R, Relvas JB, Suter U, Tricaud N.** 2010. Dlg1-PTEN interaction regulates myelin thickness to prevent damaging peripheral nerve overmyelination. *Science* **328**: 1415–1418. DOI: <https://doi.org/10.1126/science.1187735>, PMID: 20448149
- Court FA, Sherman DL, Pratt T, Garry EM, Ribchester RR, Cottrell DF, Fleetwood-Walker SM, Brophy PJ.** 2004. Restricted growth of Schwann cells lacking Cajal bands slows conduction in myelinated nerves. *Nature* **431**: 191–195. DOI: <https://doi.org/10.1038/nature02841>, PMID: 15356632
- D’Antonio M, Michalovich D, Paterson M, Droggiti A, Woodhoo A, Mirsky R, Jessen KR.** 2006. Gene profiling and bioinformatic analysis of Schwann cell embryonic development and myelination. *Glia* **53**:501–515. DOI: <https://doi.org/10.1002/glia.20309>, PMID: 16369933
- Darbas A, Jaegle M, Walbeehm E, van den Burg H, Driegen S, Broos L, Uyl M, Visser P, Grosveld F, Meijer D.** 2004. Cell autonomy of the mouse claw paw mutation. *Developmental Biology* **272**:470–482. DOI: <https://doi.org/10.1016/j.ydbio.2004.05.017>, PMID: 15282162
- de Monasterio-Schrader P, Jahn O, Tenzer S, Wichert SP, Patzig J, Werner HB.** 2012. Systematic approaches to central nervous system myelin. *Cellular and Molecular Life Sciences* **69**:2879–2894. DOI: <https://doi.org/10.1007/s00018-012-0958-9>
- de Monasterio-Schrader P, Patzig J, Möbius W, Barrette B, Wagner TL, Kusch K, Edgar JM, Brophy PJ, Werner HB.** 2013. Uncoupling of neuroinflammation from axonal degeneration in mice lacking the myelin protein tetraspanin-2. *Glia* **61**:1832–1847. DOI: <https://doi.org/10.1002/glia.22561>
- Distler U, Kuharev J, Tenzer S.** 2014a. Biomedical applications of ion mobility-enhanced data-independent acquisition-based label-free quantitative proteomics. *Expert Review of Proteomics* **11**:675–684. DOI: <https://doi.org/10.1586/14789450.2014.971114>, PMID: 25327648

- Distler U**, Kuharev J, Navarro P, Levin Y, Schild H, Tenzer S. 2014b. Drift time-specific collision energies enable deep-coverage data-independent acquisition proteomics. *Nature Methods* **11**:167–170. DOI: <https://doi.org/10.1038/nmeth.2767>
- Distler U**, Kuharev J, Navarro P, Tenzer S. 2016. Label-free quantification in ion mobility-enhanced data-independent acquisition proteomics. *Nature Protocols* **11**:795–812. DOI: <https://doi.org/10.1038/nprot.2016.042>, PMID: 27010757
- Dodds JN**, Baker ES. 2019. Ion mobility spectrometry: fundamental concepts, instrumentation, applications, and the road ahead. *Journal of the American Society for Mass Spectrometry* **30**:2185–2195. DOI: <https://doi.org/10.1007/s13361-019-02288-2>, PMID: 31493234
- Domènech-Estévez E**, Baloui H, Repond C, Rosafio K, Médard JJ, Tricaud N, Pellerin L, Chrast R. 2015. Distribution of monocarboxylate transporters in the peripheral nervous system suggests putative roles in lactate shuttling and myelination. *Journal of Neuroscience* **35**:4151–4156. DOI: <https://doi.org/10.1523/JNEUROSCI.3534-14.2015>, PMID: 25762662
- Duan X**, Gu W, Hao Y, Wang R, Wen H, Sun S, Jiao J, Fan D. 2016. A novel Asp121Asn mutation of myelin protein zero is associated with late-onset axonal Charcot-Marie-Tooth disease, hearing loss and pupil abnormalities. *Frontiers in Aging Neuroscience* **8**:00222. DOI: <https://doi.org/10.3389/fnagi.2016.00222>
- Edgar JM**, McLaughlin M, Werner HB, McCulloch MC, Barrie JA, Brown A, Faichney AB, Snaidero N, Nave KA, Griffiths IR. 2009. Early ultrastructural defects of axons and axon-glia junctions in mice lacking expression of *Cnp1*. *Glia* **57**:1815–1824. DOI: <https://doi.org/10.1002/glia.20893>, PMID: 19459211
- Erwig MS**, Hesse D, Jung RB, Uecker M, Kusch K, Tenzer S, Jahn O, Werner HB. 2019a. Myelin: Methods for Purification and Proteome Analysis. In: *Methods in Molecular Biology*. Springer. p. 37–63. DOI: https://doi.org/10.1007/978-1-4939-9072-6_3
- Erwig MS**, Patzig J, Steyer AM, Dibaj P, Heilmann M, Heilmann I, Jung RB, Kusch K, Möbius W, Jahn O, Nave KA, Werner HB. 2019b. Anillin facilitates septin assembly to prevent pathological outfoldings of central nervous system myelin. *eLife* **8**:e43888. DOI: <https://doi.org/10.7554/eLife.43888>, PMID: 30672734
- Fabrizi GM**, Tamburin S, Cavallaro T, Cabrini I, Ferrarini M, Taioli F, Magrinelli F, Zanette G. 2018. The spectrum of Charcot-Marie-Tooth disease due to myelin protein zero: an electrodiagnostic, nerve ultrasound and histological study. *Clinical Neurophysiology* **129**:21–32. DOI: <https://doi.org/10.1016/j.clinph.2017.09.117>, PMID: 29136549
- Fannon AM**, Sherman DL, Ilyina-Gragerova G, Brophy PJ, Friedrich VL, Colman DR. 1995. Novel E-cadherin-mediated adhesion in peripheral nerve: Schwann cell architecture is stabilized by autotypic adherens junctions. *Journal of Cell Biology* **129**:189–202. DOI: <https://doi.org/10.1083/jcb.129.1.189>, PMID: 7698985
- Faroni A**, Smith RJ, Procacci P, Castelnovo LF, Puccianti E, Reid AJ, Magnaghi V, Verkhatsky A. 2014. Purinergic signaling mediated by P2X7 receptors controls myelination in sciatic nerves. *Journal of Neuroscience Research* **92**:1259–1328. DOI: <https://doi.org/10.1002/jnr.23417>, PMID: 24903685
- Feltri ML**, Graus Porta D, Previtali SC, Nodari A, Migliavacca B, Cassetti A, Littlewood-Evans A, Reichardt LF, Messing A, Quattrini A, Mueller U, Wrabetz L. 2002. Conditional disruption of beta 1 integrin in Schwann cells impedes interactions with axons. *Journal of Cell Biology* **156**:199–210. DOI: <https://doi.org/10.1083/jcb.200109021>, PMID: 11777940
- Feltri ML**, Poitelon Y, Previtali SC. 2016. How Schwann cells sort axons. *The Neuroscientist* **22**:252–265. DOI: <https://doi.org/10.1177/1073858415572361>
- Fernandez-Valle C**, Tang Y, Ricard J, Rodenas-Ruano A, Taylor A, Hackler E, Biggerstaff J, Iacovelli J. 2002. Paxillin binds schwannomin and regulates its density-dependent localization and effect on cell morphology. *Nature Genetics* **31**:354–362. DOI: <https://doi.org/10.1038/ng930>, PMID: 12118253
- Figlewicz DA**, Quarles RH, Johnson D, Barbarash GR, Sternberger NH. 1981. Biochemical demonstration of the myelin-associated glycoprotein in the peripheral nervous system. *Journal of Neurochemistry* **37**:749–758. DOI: <https://doi.org/10.1111/j.1471-4159.1982.tb12551.x>, PMID: 6168745
- Fledrich R**, Abdelaal T, Rasch L, Bansal V, Schütza V, Brügger B, Luchtenborg C, Prukop T, Stenzel J, Rahman RU, Hermes D, Ewers D, Möbius W, Ruhwedel T, Katona I, Weis J, Klein D, Martini R, Brück W, Müller WC, et al. 2018. Targeting myelin lipid metabolism as a potential therapeutic strategy in a model of CMT1A neuropathy. *Nature Communications* **9**:3025. DOI: <https://doi.org/10.1038/s41467-018-05420-0>, PMID: 30072689
- Fuhrmann-Stroissnigg H**, Noiges R, Descovich L, Fischer I, Albrecht DE, Nothias F, Froehner SC, Propst F. 2012. The light chains of microtubule-associated proteins MAP1A and MAP1B interact with α 1-syntrophin in the central and peripheral nervous system. *PLOS ONE* **7**:e49722. DOI: <https://doi.org/10.1371/journal.pone.0049722>, PMID: 23152929
- Funabashi K**, Okada N, Matsuo S, Yamamoto T, Morgan BP, Okada H. 1994. Tissue distribution of complement regulatory membrane proteins in rats. *Immunology* **81**:444–495. PMID: 7515849
- Fünfschilling U**, Supplie LM, Mahad D, Boretius S, Saab AS, Edgar J, Brinkmann BG, Kassmann CM, Tzvetanova ID, Möbius W, Diaz F, Meijer D, Suter U, Hamprecht B, Sereda MW, Moraes CT, Frahm J, Goebbels S, Nave KA. 2012. Glycolytic oligodendrocytes maintain myelin and long-term axonal integrity. *Nature* **485**:517–521. DOI: <https://doi.org/10.1038/nature11007>, PMID: 22622581
- Gallardo E**, García A, Ramón C, Maraví E, Infante J, Gastón I, Alonso Á, Combarros O, De Jonghe P, Berciano J. 2009. Charcot-Marie-Tooth disease type 2J with MPZ Thr124Met mutation: clinico-electrophysiological and MRI study of a family. *Journal of Neurology* **256**:2061–2071. DOI: <https://doi.org/10.1007/s00415-009-5251-y>, PMID: 19629567

- Garbern JY**, Cambi F, Tang XM, Sima AA, Vallat JM, Bosch EP, Lewis R, Shy M, Sohi J, Kraft G, Chen KL, Joshi I, Leonard DG, Johnson W, Raskind W, Dlouhy SR, Pratt V, Hodes ME, Bird T, Kamholz J. 1997. Proteolipid protein is necessary in peripheral as well as central myelin. *Neuron* **19**:205–218. DOI: [https://doi.org/10.1016/S0896-6273\(00\)80360-8](https://doi.org/10.1016/S0896-6273(00)80360-8), PMID: 9247276
- Geromanos SJ**, Vissers JP, Silva JC, Dorschel CA, Li GZ, Gorenstein MV, Bateman RH, Langridge JI. 2009. The detection, correlation, and comparison of peptide precursor and product ions from data independent LC-MS with data dependant LC-MS/MS. *Proteomics* **9**:1683–1695. DOI: <https://doi.org/10.1002/pmic.200800562>, PMID: 19294628
- Ghidinelli M**, Poitelon Y, Shin YK, Ameroso D, Williamson C, Ferri C, Pellegatta M, Espino K, Mogha A, Monk K, Podini P, Taveggia C, Nave KA, Wrabetz L, Park HT, Feltri ML. 2017. Laminin 211 inhibits protein kinase A in Schwann cells to modulate neuregulin 1 type III-driven myelination. *PLOS Biology* **15**:e2001408. DOI: <https://doi.org/10.1371/journal.pbio.2001408>, PMID: 28636612
- Giese KP**, Martini R, Lemke G, Soriano P, Schachner M. 1992. Mouse P0 gene disruption leads to Hypomyelination, abnormal expression of recognition molecules, and degeneration of myelin and axons. *Cell* **71**:565–576. DOI: [https://doi.org/10.1016/0092-8674\(92\)90591-Y](https://doi.org/10.1016/0092-8674(92)90591-Y), PMID: 1384988
- Gillespie CS**, Sherman DL, Blair GE, Brophy PJ. 1994. Periaxin, a novel protein of myelinating Schwann cells with a possible role in axonal ensheathment. *Neuron* **12**:497–508. DOI: [https://doi.org/10.1016/0896-6273\(94\)90208-9](https://doi.org/10.1016/0896-6273(94)90208-9), PMID: 8155317
- Gillespie CS**, Sherman DL, Fleetwood-Walker SM, Cottrell DF, Tait S, Garry EM, Wallace VC, Ure J, Griffiths IR, Smith A, Brophy PJ. 2000. Peripheral demyelination and neuropathic pain behavior in periaxin-deficient mice. *Neuron* **26**:523–531. DOI: [https://doi.org/10.1016/S0896-6273\(00\)81184-8](https://doi.org/10.1016/S0896-6273(00)81184-8), PMID: 10839370
- Gitik M**, Liraz-Zaltsman S, Oldenborg PA, Reichert F, Rotshenker S. 2011. Myelin down-regulates myelin phagocytosis by microglia and macrophages through interactions between CD47 on myelin and SIRP α (signal regulatory protein- α) on phagocytes. *Journal of Neuroinflammation* **8**:24. DOI: <https://doi.org/10.1186/1742-2094-8-24>, PMID: 21401967
- Gonçalves AF**, Dias NG, Moransard M, Correia R, Pereira JA, Witke W, Suter U, Relvas JB. 2010. Gelsolin is required for macrophage recruitment during remyelination of the peripheral nervous system. *Glia* **58**:706–721. DOI: <https://doi.org/10.1002/glia.20956>, PMID: 20014276
- Gonçalves NP**, Vægter CB, Andersen H, Østergaard L, Calcutt NA, Jensen TS. 2017. Schwann cell interactions with axons and microvessels in diabetic neuropathy. *Nature Reviews Neurology* **13**:135–147. DOI: <https://doi.org/10.1038/nrneuro.2016.201>, PMID: 28134254
- Greenfield S**, Brostoff S, Eylar EH, Morell P. 1973. Protein composition of myelin of the peripheral nervous system. *Journal of Neurochemistry* **20**:1207–1216. DOI: <https://doi.org/10.1111/j.1471-4159.1973.tb00089.x>, PMID: 4697881
- Grove M**, Brophy PJ. 2014. FAK is required for Schwann cell spreading on immature basal Lamina to coordinate the radial sorting of peripheral axons with myelination. *Journal of Neuroscience* **34**:13422–13434. DOI: <https://doi.org/10.1523/JNEUROSCI.1764-14.2014>, PMID: 25274820
- Guilbot A**, Williams A, Ravisé N, Verny C, Brice A, Sherman DL, Brophy PJ, LeGuern E, Delague V, Bareil C, Mégarbané A, Claustres M. 2001. A mutation in periaxin is responsible for CMT4F, an autosomal recessive form of Charcot-Marie-Tooth disease. *Human Molecular Genetics* **10**:415–421. DOI: <https://doi.org/10.1093/hmg/10.4.415>, PMID: 11157804
- Hartline DK**, Colman DR. 2007. Rapid conduction and the evolution of giant axons and myelinated fibers. *Current Biology* **17**:R29–R35. DOI: <https://doi.org/10.1016/j.cub.2006.11.042>, PMID: 17208176
- Hayashi A**, Nakashima K, Yamagishi K, Hoshi T, Suzuki A, Baba H. 2007. Localization of annexin II in the paranodal regions and Schmidt-Lanterman incisures in the peripheral nervous system. *Glia* **55**:1044–1052. DOI: <https://doi.org/10.1002/glia.20529>, PMID: 17549680
- Hess A**, Lansing AI. 1953. The fine structure of peripheral nerve fibers. *The Anatomical Record* **117**:175–199. DOI: <https://doi.org/10.1002/ar.1091170205>, PMID: 13104987
- Hulsen T**, de Vlieg J, Alkema W. 2008. BioVenn - a web application for the comparison and visualization of biological lists using area-proportional venn diagrams. *BMC Genomics* **9**:488. DOI: <https://doi.org/10.1186/1471-2164-9-488>, PMID: 18925949
- Ishibashi T**, Ding L, Ikenaka K, Inoue Y, Miyado K, Mekada E, Baba H. 2004. Tetraspanin protein CD9 is a novel paranodal component regulating paranodal junctional formation. *Journal of Neuroscience* **24**:96–102. DOI: <https://doi.org/10.1523/JNEUROSCI.1484-03.2004>, PMID: 14715942
- Ishimoto T**, Ninomiya K, Inoue R, Koike M, Uchiyama Y, Mori H. 2017. Mice lacking BCAS1, a novel myelin-associated protein, display hypomyelination, schizophrenia-like abnormal behaviors, and upregulation of inflammatory genes in the brain. *Glia* **65**:727–739. DOI: <https://doi.org/10.1002/glia.23129>, PMID: 28230289
- Ivanovic A**, Horresh I, Golan N, Spiegel I, Sabanay H, Frechter S, Ohno S, Terada N, Möbius W, Rosenbluth J, Brose N, Peles E. 2012. The cytoskeletal adapter protein 4.1G organizes the internodes in peripheral myelinated nerves. *Journal of Cell Biology* **196**:337–344. DOI: <https://doi.org/10.1083/jcb.201111127>, PMID: 22291039
- Jahn O**, Tenzer S, Werner HB. 2009. Myelin proteomics: molecular anatomy of an insulating sheath. *Molecular Neurobiology* **40**:55–72. DOI: <https://doi.org/10.1007/s12035-009-8071-2>, PMID: 19452287
- Jha MK**, Lee Y, Russell KA, Yang F, Dastgheyb RM, Deme P, Ament XH, Chen W, Liu Y, Guan Y, Polydefkis MJ, Hoke A, Haughey NJ, Rothstein JD, Morrison BM. 2020. Monocarboxylate transporter 1 in Schwann cells contributes to maintenance of sensory nerve myelination during aging. *Glia* **68**:161–177. DOI: <https://doi.org/10.1002/glia.23710>, PMID: 31453649

- Jung M**, Sommer I, Schachner M, Nave KA. 1996. Monoclonal antibody O10 defines a conformationally sensitive cell-surface epitope of proteolipid protein (PLP): evidence that PLP misfolding underlies dysmyelination in mutant mice. *Journal of Neuroscience* **16**:7920–7929. DOI: <https://doi.org/10.1523/JNEUROSCI.16-24-07920.1996>, PMID: 8987820
- Kabzinska D**, Drac H, Sherman DL, Kostera-Pruszczyk A, Brophy PJ, Kochanski A, Hausmanowa-Petrusewicz I. 2006. Charcot-Marie-Tooth type 4F disease caused by S399fsx410 mutation in the PRX gene. *Neurology* **66**:745–747. DOI: <https://doi.org/10.1212/01.wnl.0000201269.46071.35>, PMID: 16534116
- Kammers K**, Cole RN, Tiengwe C, Ruczinski I. 2015. Detecting significant changes in protein abundance. *EuPA Open Proteomics* **7**:11–19. DOI: <https://doi.org/10.1016/j.euprot.2015.02.002>, PMID: 25821719
- Kangas SM**, Ohlmeier S, Sormunen R, Jouhilahti EM, Peltonen S, Peltonen J, Heape AM. 2016. An approach to comprehensive genome and proteome expression analyses in Schwann cells and neurons during peripheral nerve myelin formation. *Journal of Neurochemistry* **138**:830–844. DOI: <https://doi.org/10.1111/jnc.13722>, PMID: 27364987
- Kim S**, Maynard JC, Sasaki Y, Strickland A, Sherman DL, Brophy PJ, Burlingame AL, Milbrandt J. 2016. Schwann cell O-GlcNAc glycosylation is required for myelin maintenance and axon integrity. *Journal of Neuroscience* **36**:9633–9646. DOI: <https://doi.org/10.1523/JNEUROSCI.1235-16.2016>, PMID: 27629714
- Kleopa KA**, Sargiannidou I. 2015. Connexins, gap junctions and peripheral neuropathy. *Neuroscience Letters* **596**:27–32. DOI: <https://doi.org/10.1016/j.neulet.2014.10.033>, PMID: 25449862
- Kuharev J**, Navarro P, Distler U, Jahn O, Tenzer S. 2015. In-depth evaluation of software tools for data-independent acquisition based label-free quantification. *Proteomics* **15**:3140–3151. DOI: <https://doi.org/10.1002/pmic.201400396>, PMID: 25545627
- Kusch K**, Uecker M, Liepold T, Möbius W, Hoffmann C, Neumann H, Werner H, Jahn O. 2017. Partial immunoblotting of 2D-Gels: a novel method to identify post-translationally modified proteins exemplified for the myelin acetylome. *Proteomes* **5**:3. DOI: <https://doi.org/10.3390/proteomes5010003>
- Larocca JN**, Norton WT. 2006. Isolation of myelin. *Current Protocols in Cell Biology* **33**:3.25.1–3.25.3. DOI: <https://doi.org/10.1002/0471143030.cb0325s33>
- Le N**, Nagarajan R, Wang JYT, Araki T, Schmidt RE, Milbrandt J. 2005. Analysis of congenital hypomyelinating Egr2Lo/Lo nerves identifies Sox2 as an inhibitor of Schwann cell differentiation and myelination. *PNAS* **102**:2596–2601. DOI: <https://doi.org/10.1073/pnas.0407836102>
- Leal A**, Berghoff C, Berghoff M, Rojas-Araya M, Ortiz C, Heuss D, Rautenstrauss B. 2014. A Costa Rican family affected with Charcot-Marie-Tooth disease due to the myelin protein zero (MPZ) p.Thr124Met mutation shares the Belgian haplotype. *Revista De Biología Tropical* **62**:1285. DOI: <https://doi.org/10.15517/rbt.v62i4.13473>
- LeBeau JM**, Liuzzi FJ, Depto AS, Vinik AI. 1994. Differential laminin gene expression in dorsal root ganglion neurons and nonneuronal cells. *Experimental Neurology* **127**:1–8. DOI: <https://doi.org/10.1006/exnr.1994.1074>, PMID: 8200428
- Lee HK**, Seo IA, Park HK, Park YM, Ahn KJ, Yoo YH, Park HT. 2007. Nidogen is a prosurvival and promigratory factor for adult Schwann cells. *Journal of Neurochemistry* **102**:686–698. DOI: <https://doi.org/10.1111/j.1471-4159.2007.04580.x>, PMID: 17437540
- Lee Y**, Morrison BM, Li Y, Lengacher S, Farah MH, Hoffman PN, Liu Y, Tsingalia A, Jin L, Zhang PW, Pellerin L, Magistretti PJ, Rothstein JD. 2012. Oligodendroglia metabolically support axons and contribute to neurodegeneration. *Nature* **487**:443–448. DOI: <https://doi.org/10.1038/nature11314>, PMID: 22801498
- Lee S**, Amici S, Tavori H, Zeng WM, Freeland S, Fazio S, Notterpek L. 2014. PMP22 is critical for actin-mediated cellular functions and for establishing lipid rafts. *Journal of Neuroscience* **34**:16140–16152. DOI: <https://doi.org/10.1523/JNEUROSCI.1908-14.2014>, PMID: 25429154
- Li X**, Lynn BD, Olson C, Meier C, Davidson KG, Yasumura T, Rash JE, Nagy JI. 2002. Connexin29 expression, immunocytochemistry and freeze-fracture replica immunogold labelling (FRIL) in sciatic nerve. *European Journal of Neuroscience* **16**:795–806. DOI: <https://doi.org/10.1046/j.1460-9568.2002.02149.x>, PMID: 12372015
- Li GZ**, Vissers JP, Silva JC, Golick D, Gorenstein MV, Geromanos SJ. 2009. Database searching and accounting of multiplexed precursor and product ion spectra from the data independent analysis of simple and complex peptide mixtures. *Proteomics* **9**:1696–1719. DOI: <https://doi.org/10.1002/pmic.200800564>, PMID: 19294629
- Lin HH**, Snyder BS, Connor JR. 1990. Transferrin expression in myelinated and non-myelinated peripheral nerves. *Brain Research* **526**:217–220. DOI: [https://doi.org/10.1016/0006-8993\(90\)91224-5](https://doi.org/10.1016/0006-8993(90)91224-5), PMID: 2257482
- Liu Y**, Oppenheim RW, Sugiura Y, Lin W. 2009. Abnormal development of the neuromuscular junction in Nedd4-deficient mice. *Developmental Biology* **330**:153–166. DOI: <https://doi.org/10.1016/j.ydbio.2009.03.023>, PMID: 19345204
- Mantuano E**, Lam MS, Shibayama M, Campana WM, Gonias SL. 2015. The NMDA receptor functions independently and as an LRP1 co-receptor to promote Schwann cell survival and migration. *Journal of Cell Science* **128**:3478–3488. DOI: <https://doi.org/10.1242/jcs.173765>, PMID: 26272917
- Marchesi C**, Milani M, Morbin M, Cesani M, Lauria G, Scafoli V, Piccolo G, Fabrizi GM, Cavallaro T, Taroni F, Pareyson D. 2010. Four novel cases of periaxin-related neuropathy and review of the literature. *Neurology* **75**:1830–1838. DOI: <https://doi.org/10.1212/WNL.0b013e3181fd6314>, PMID: 21079185
- Marques S**, Zeisel A, Codeluppi S, van Bruggen D, Mendanha Falcão A, Xiao L, Li H, Häring M, Hochgerner H, Romanov RA, Gyllborg D, Muñoz Manchado A, La Manno G, Lönnerberg P, Floriddia EM, Rezayee F, Ernfors P, Arenas E, Hjerling-Leffler J, Harkany T, et al. 2016. Oligodendrocyte heterogeneity in the mouse juvenile and adult central nervous system. *Science* **352**:1326–1329. DOI: <https://doi.org/10.1126/science.aaf6463>, PMID: 27284195

- Martini R**, Mohajeri MH, Kasper S, Giese KP, Schachner M. 1995. Mice doubly deficient in the genes for P0 and myelin basic protein show that both proteins contribute to the formation of the major dense line in peripheral nerve myelin. *Journal of Neuroscience* **15**:4488–4495. DOI: <https://doi.org/10.1523/JNEUROSCI.15-06-04488.1995>, PMID: 7540676
- Masaki T**, Matsumura K, Hirata A, Yamada H, Hase A, Arai K, Shimizu T, Yorifuji H, Motoyoshi K, Kamakura K. 2002. Expression of dystroglycan and the laminin-alpha 2 chain in the rat peripheral nerve during development. *Experimental Neurology* **174**:109–117. DOI: <https://doi.org/10.1006/exnr.2001.7856>, PMID: 11869039
- Mathieu JM**, Costantino-Ceccarini E, Bény M, Reigner J. 1980. Evidence for the association of 2',3'-cyclic-nucleotide 3'-phosphodiesterase with myelin-related membranes in peripheral nervous system. *Journal of Neurochemistry* **35**:1345–1350. DOI: <https://doi.org/10.1111/j.1471-4159.1980.tb09008.x>, PMID: 6255099
- Michailov GV**, Sereda MW, Brinkmann BG, Fischer TM, Haug B, Birchmeier C, Role L, Lai C, Schwab MH, Nave KA. 2004. Axonal neuregulin-1 regulates myelin sheath thickness. *Science* **304**:700–703. DOI: <https://doi.org/10.1126/science.1095862>, PMID: 15044753
- Micko S**, Schlaepfer WW. 1978. Protein composition of axons and myelin from rat and human peripheral nerves. *Journal of Neurochemistry* **30**:1041–1049. DOI: <https://doi.org/10.1111/j.1471-4159.1978.tb12397.x>, PMID: 666897
- Mikol DD**, Scherer SS, Duckett SJ, Hong HL, Feldman EL. 2002. Schwann cell caveolin-1 expression increases during myelination and decreases after axotomy. *Glia* **38**:191–199. DOI: <https://doi.org/10.1002/glia.10063>, PMID: 11968057
- Miyamoto T**, Morita K, Takemoto D, Takeuchi K, Kitano Y, Miyakawa T, Nakayama K, Okamura Y, Sasaki H, Miyachi Y, Furuse M, Tsukita S. 2005. Tight junctions in Schwann cells of peripheral myelinated axons: a lesson from claudin-19-deficient mice. *The Journal of Cell Biology* **169**:527–565. DOI: <https://doi.org/10.1083/jcb.200501154>, PMID: 15883201
- Monk KR**, Naylor SG, Glenn TD, Mercurio S, Perlin JR, Dominguez C, Moens CB, Talbot WS. 2009. A G protein-coupled receptor is essential for Schwann cells to initiate myelination. *Science* **325**:1402–1405. DOI: <https://doi.org/10.1126/science.1173474>, PMID: 19745155
- Monk KR**, Oshima K, Jörs S, Heller S, Talbot WS. 2011. Gpr126 is essential for peripheral nerve development and myelination in mammals. *Development* **138**:2673–2680. DOI: <https://doi.org/10.1242/dev.062224>, PMID: 21613327
- Monk KR**, Feltri ML, Taveggia C. 2015. New insights on Schwann cell development. *Glia* **63**:1376–1393. DOI: <https://doi.org/10.1002/glia.22852>, PMID: 25921593
- Montani L**, Buerki-Thurnherr T, de Faria JP, Pereira JA, Dias NG, Fernandes R, Gonçalves AF, Braun A, Benninger Y, Böttcher RT, Costell M, Nave KA, Franklin RJ, Meijer D, Suter U, Relvas JB. 2014. Profilin 1 is required for peripheral nervous system myelination. *Development* **141**:1553–1561. DOI: <https://doi.org/10.1242/dev.101840>, PMID: 24598164
- Morrison BM**, Lee Y, Rothstein JD. 2013. Oligodendroglia: metabolic supporters of axons. *Trends in Cell Biology* **23**:644–651. DOI: <https://doi.org/10.1016/j.tcb.2013.07.007>
- Morrison BM**, Tsingalia A, Vidensky S, Lee Y, Jin L, Farah MH, Lengacher S, Magistretti PJ, Pellerin L, Rothstein JD. 2015. Deficiency in monocarboxylate transporter 1 (MCT1) in mice delays regeneration of peripheral nerves following sciatic nerve crush. *Experimental Neurology* **263**:325–338. DOI: <https://doi.org/10.1016/j.expneurol.2014.10.018>, PMID: 25447940
- Murata M**, Shibuya Y, Munemoto S, Takeuchi J, Kobayashi M, Suzuki H, Komori T. 2006. Ultrastructural localization of alpha E-catenin in the rat sciatic nerve. *The Kobe Journal of Medical Sciences* **52**:77–84. PMID: 16855370
- Myllykoski M**, Eichel MA, Jung RB, Kelm S, Werner HB, Kursula P. 2018. High-affinity heterotetramer formation between the large myelin-associated glycoprotein and the dynein light chain DYNLL1. *Journal of Neurochemistry* **147**:764–783. DOI: <https://doi.org/10.1111/jnc.14598>, PMID: 30261098
- Nagarajan R**, Le N, Mahoney H, Araki T, Milbrandt J. 2002. Deciphering peripheral nerve myelination by using Schwann cell expression profiling. *PNAS* **99**:8998–9003. DOI: <https://doi.org/10.1073/pnas.132080999>, PMID: 12084938
- Nave KA**, Werner HB. 2014. Myelination of the nervous system: mechanisms and functions. *Annual Review of Cell and Developmental Biology* **30**:503–533. DOI: <https://doi.org/10.1146/annurev-cellbio-100913-013101>, PMID: 25288117
- Nawaz S**, Schweitzer J, Jahn O, Werner HB. 2013. Molecular evolution of myelin basic protein, an abundant structural myelin component. *Glia* **61**:1364–1377. DOI: <https://doi.org/10.1002/glia.22520>, PMID: 24040667
- Neilson KA**, Ali NA, Muralidharan S, Mirzaei M, Mariani M, Assadourian G, Lee A, van Sluyter SC, Haynes PA. 2011. Less label, more free: approaches in label-free quantitative mass spectrometry. *Proteomics* **11**:535–553. DOI: <https://doi.org/10.1002/pmic.201000553>, PMID: 21243637
- Nodari A**, Previtali SC, Dati G, Occhi S, Court FA, Colombelli C, Zambroni D, Dina G, Del Carro U, Campbell KP, Quattrini A, Wrabetz L, Feltri ML. 2008. Alpha6 beta4 integrin and dystroglycan cooperate to stabilize the myelin sheath. *Journal of Neuroscience* **28**:6714–6719. DOI: <https://doi.org/10.1523/JNEUROSCI.0326-08.2008>, PMID: 18579745
- Ogata T**, Iijima S, Hoshikawa S, Miura T, Yamamoto S, Oda H, Nakamura K, Tanaka S. 2004. Opposing extracellular signal-regulated kinase and akt pathways control Schwann cell myelination. *Journal of Neuroscience* **24**:6724–6732. DOI: <https://doi.org/10.1523/JNEUROSCI.5520-03.2004>, PMID: 15282275

- Ohno N**, Terada N, Yamakawa H, Komada M, Ohara O, Trapp BD, Ohno S. 2006. Expression of protein 4.1G in Schwann cells of the peripheral nervous system. *Journal of Neuroscience Research* **84**:568–577. DOI: <https://doi.org/10.1002/jnr.20949>, PMID: 16752423
- Pareyson D**, Marchesi C. 2009. Diagnosis, natural history, and management of Charcot-Marie-Tooth disease. *The Lancet Neurology* **8**:654–667. DOI: [https://doi.org/10.1016/S1474-4422\(09\)70110-3](https://doi.org/10.1016/S1474-4422(09)70110-3), PMID: 19539237
- Patzig J**, Jahn O, Tenzer S, Wichert SP, de Monasterio-Schrader P, Rosfa S, Kuharev J, Yan K, Bormuth I, Bremer J, Aguzzi A, Orfaniotou F, Hesse D, Schwab MH, Möbius W, Nave KA, Werner HB. 2011. Quantitative and integrative proteome analysis of peripheral nerve myelin identifies novel myelin proteins and candidate neuropathy loci. *Journal of Neuroscience* **31**:16369–16386. DOI: <https://doi.org/10.1523/JNEUROSCI.4016-11.2011>, PMID: 22072688
- Patzig J**, Kusch K, Fledrich R, Eichel MA, Lüders KA, Möbius W, Sereda MW, Nave K-A, Martini R, Werner HB. 2016a. Proteolipid protein modulates preservation of peripheral axons and premature death when myelin protein zero is lacking. *Glia* **64**:155–174. DOI: <https://doi.org/10.1002/glia.22922>
- Patzig J**, Erwig MS, Tenzer S, Kusch K, Dibaj P, Möbius W, Goebbels S, Schaeren-Wiemers N, Nave KA, Werner HB. 2016b. Septin/anillin filaments scaffold central nervous system myelin to accelerate nerve conduction. *eLife* **5**:e17119. DOI: <https://doi.org/10.7554/eLife.17119>, PMID: 27504968
- Pereira JA**, Lebrun-Julien F, Suter U. 2012. Molecular mechanisms regulating myelination in the peripheral nervous system. *Trends in Neurosciences* **35**:123–134. DOI: <https://doi.org/10.1016/j.tins.2011.11.006>, PMID: 22192173
- Petersen SC**, Luo R, Liebscher I, Giera S, Jeong SJ, Mogha A, Ghidinelli M, Feltri ML, Schöneberg T, Piao X, Monk KR. 2015. The adhesion GPCR GPR126 has distinct, domain-dependent functions in Schwann cell development mediated by interaction with laminin-211. *Neuron* **85**:755–769. DOI: <https://doi.org/10.1016/j.neuron.2014.12.057>, PMID: 25695270
- Philp NJ**, Ochrietor JD, Rudoy C, Muramatsu T, Linser PJ. 2003. Loss of MCT1, MCT3, and MCT4 expression in the retinal pigment epithelium and neural retina of the 5a11/Basigin-Null mouse. *Investigative Ophthalmology & Visual Science* **44**:1305. DOI: <https://doi.org/10.1167/iovs.02-0552>
- Poliak S**, Matlis S, Ullmer C, Scherer SS, Peles E. 2002. Distinct claudins and associated PDZ proteins form different autotypic tight junctions in myelinating Schwann cells. *Journal of Cell Biology* **159**:361–372. DOI: <https://doi.org/10.1083/jcb.200207050>, PMID: 12403818
- Quattrini A**, Previtali S, Feltri ML, Canal N, Nemni R, Wrabetz L. 1996. Beta 4 integrin and other Schwann cell markers in axonal neuropathy. *Glia* **17**:294–306. DOI: [https://doi.org/10.1002/\(SICI\)1098-1136\(199608\)17:4<294::AID-GLIA4>3.0.CO;2-#](https://doi.org/10.1002/(SICI)1098-1136(199608)17:4<294::AID-GLIA4>3.0.CO;2-#), PMID: 8856326
- Raasakka A**, Linxweiler H, Brophy PJ, Sherman DL, Kursula P. 2019. Direct binding of the flexible C-Terminal segment of periaxin to $\beta 4$ integrin suggests a molecular basis for CMT4F. *Frontiers in Molecular Neuroscience* **12**:84. DOI: <https://doi.org/10.3389/fnmol.2019.00084>
- Rende M**, Muir D, Ruoslahti E, Hagg T, Varon S, Manthorpe M. 1992. Immunolocalization of ciliary neuronotrophic factor in adult rat sciatic nerve. *Glia* **5**:25–32. DOI: <https://doi.org/10.1002/glia.440050105>, PMID: 1531807
- Riethmacher D**, Sonnenberg-Riethmacher E, Brinkmann V, Yamaai T, Lewin GR, Birchmeier C. 1997. Severe neuropathies in mice with targeted mutations in the ErbB3 receptor. *Nature* **389**:725–730. DOI: <https://doi.org/10.1038/39593>, PMID: 9338783
- Rinholm JE**, Bergersen LH. 2014. White matter lactate—does it matter? *Neuroscience* **276**:109–116. DOI: <https://doi.org/10.1016/j.neuroscience.2013.10.002>, PMID: 24125892
- Ritchie ME**, Phipson B, Wu D, Hu Y, Law CW, Shi W, Smyth GK. 2015. Limma powers differential expression analyses for RNA-sequencing and microarray studies. *Nucleic Acids Research* **43**:e47. DOI: <https://doi.org/10.1093/nar/gkv007>, PMID: 25605792
- Rossor AM**, Polke JM, Houlden H, Reilly MM. 2013. Clinical implications of genetic advances in Charcot-Marie-Tooth disease. *Nature Reviews Neurology* **9**:562–571. DOI: <https://doi.org/10.1038/nrneuro.2013.179>, PMID: 24018473
- Ryu EJ**, Yang M, Gustin JA, Chang LW, Freimuth RR, Nagarajan R, Milbrandt J. 2008. Analysis of peripheral nerve expression profiles identifies a novel myelin glycoprotein, MP11. *Journal of Neuroscience* **28**:7563–7573. DOI: <https://doi.org/10.1523/JNEUROSCI.1659-08.2008>, PMID: 18650334
- Saab AS**, Tzvetanova ID, Nave KA. 2013. The role of myelin and oligodendrocytes in axonal energy metabolism. *Current Opinion in Neurobiology* **23**:1065–1072. DOI: <https://doi.org/10.1016/j.conb.2013.09.008>, PMID: 24094633
- Saitoh Y**, Ohno N, Yamauchi J, Sakamoto T, Terada N. 2017. Deficiency of a membrane skeletal protein, 4.1G, results in myelin abnormalities in the peripheral nervous system. *Histochemistry and Cell Biology* **148**:597–606. DOI: <https://doi.org/10.1007/s00418-017-1600-6>, PMID: 28755316
- Saitoh Y**, Kamijo A, Yamauchi J, Sakamoto T, Terada N. 2019. The membrane palmitoylated protein, MPP6, is involved in myelin formation in the mouse peripheral nervous system. *Histochemistry and Cell Biology* **151**:385–394. DOI: <https://doi.org/10.1007/s00418-018-1745-y>, PMID: 30357511
- Salles J**, Sargueil F, Knoll-Gellida A, Witters LA, Shy M, Jiang H, Cassagne C, Garbay B. 2002. Fatty acid synthase expression during peripheral nervous system myelination. *Molecular Brain Research* **101**:52–58. DOI: [https://doi.org/10.1016/S0169-328X\(02\)00161-4](https://doi.org/10.1016/S0169-328X(02)00161-4), PMID: 12007831
- Schaeren-Wiemers N**, Bonnet A, Erb M, Erne B, Bartsch U, Kern F, Mantei N, Sherman D, Suter U. 2004. The raft-associated protein MAL is required for maintenance of proper axon–glia interactions in the central nervous system. *Journal of Cell Biology* **166**:731–742. DOI: <https://doi.org/10.1083/jcb.200406092>, PMID: 15337780

- Schardt A**, Brinkmann BG, Mitkovski M, Sereda MW, Werner HB, Nave KA. 2009. The SNARE protein SNAP-29 interacts with the GTPase Rab3A: implications for membrane trafficking in myelinating Glia. *Journal of Neuroscience Research* **87**:3465–3479. DOI: <https://doi.org/10.1002/jnr.22005>, PMID: 19170188
- Scheiermann C**, Meda P, Aurrand-Lions M, Madani R, Yiangou Y, Coffey P, Salt TE, Ducrest-Gay D, Caille D, Howell O, Reynolds R, Lobrinus A, Adams RH, Yu AS, Anand P, Imhof BA, Nourshargh S. 2007. Expression and function of junctional adhesion molecule-C in myelinated peripheral nerves. *Science* **318**:1472–1475. DOI: <https://doi.org/10.1126/science.1149276>, PMID: 18048693
- Scherer SS**, Xu T, Crino P, Arroyo EJ, Gutmann DH. 2001. Ezrin, radixin, and moesin are components of Schwann cell microvilli. *Journal of Neuroscience Research* **65**:150–164. DOI: <https://doi.org/10.1002/jnr.1138>, PMID: 11438984
- Sharma K**, Schmitt S, Bergner CG, Tyanova S, Kannaiyan N, Manrique-Hoyos N, Kongi K, Cantuti L, Hanisch UK, Philips MA, Rossner MJ, Mann M, Simons M. 2015. Cell type- and brain region-resolved mouse brain proteome. *Nature Neuroscience* **18**:1819–1831. DOI: <https://doi.org/10.1038/nn.4160>, PMID: 26523646
- Sherman DL**, Fabrizi C, Gillespie CS, Brophy PJ. 2001. Specific disruption of a Schwann cell dystrophin-related protein complex in a demyelinating neuropathy. *Neuron* **30**:677–687. DOI: [https://doi.org/10.1016/S0896-6273\(01\)00327-0](https://doi.org/10.1016/S0896-6273(01)00327-0), PMID: 11430802
- Sherman DL**, Brophy PJ. 2005. Mechanisms of axon ensheathment and myelin growth. *Nature Reviews Neuroscience* **6**:683–690. DOI: <https://doi.org/10.1038/nrn1743>, PMID: 16136172
- Shih IM**, Nesbit M, Herlyn M, Kurman RJ. 1998. A new Mel-CAM (CD146)-specific monoclonal antibody, MN-4, on paraffin-embedded tissue. *Modern Pathology* **11**:1098–1204. PMID: 9831208
- Silva JC**, Gorenstein MV, Li G-Z, Vissers JPC, Geromanos SJ. 2006. Absolute quantification of proteins by LCMS E. *Molecular & Cellular Proteomics* **5**:144–156. DOI: <https://doi.org/10.1074/mcp.M500230-MCP200>
- Smith ME**, Curtis BM. 1979. Frog sciatic nerve myelin: a chemical characterization. *Journal of Neurochemistry* **33**:447–452. DOI: <https://doi.org/10.1111/j.1471-4159.1979.tb05174.x>, PMID: 112219
- Sparrow N**, Manetti ME, Bott M, Fabianac T, Petrilli A, Bates ML, Bunge MB, Lambert S, Fernandez-Valle C. 2012. The actin-severing protein cofilin is downstream of neuregulin signaling and is essential for Schwann cell myelination. *Journal of Neuroscience* **32**:5284–5297. DOI: <https://doi.org/10.1523/JNEUROSCI.6207-11.2012>, PMID: 22496574
- Spiegel I**, Adamsky K, Eshed Y, Milo R, Sabanay H, Sarig-Nadir O, Horresh I, Scherer SS, Rasband MN, Peles E. 2007. A central role for Necl4 (SynCAM4) in schwann cell-axon interaction and myelination. *Nature Neuroscience* **10**:861–869. DOI: <https://doi.org/10.1038/nn1915>, PMID: 17558405
- Stassart RM**, Möbius W, Nave K-A, Edgar JM. 2018. The axon-myelin unit in development and degenerative disease. *Frontiers in Neuroscience* **12**:00467. DOI: <https://doi.org/10.3389/fnins.2018.00467>
- Storey JD**. 2003. The positive false discovery rate: a Bayesian interpretation and the q -value. *The Annals of Statistics* **31**:2013–2035. DOI: <https://doi.org/10.1214/aos/1074290335>
- Stumpf SK**, Berghoff SA, Trevisiol A, Spieth L, Düking T, Schneider LV, Schlaphoff L, Dreha-Kulaczewski S, Bley A, Burfeind D, Kusch K, Mitkovski M, Ruhwedel T, Guder P, Röhse H, Denecke J, Gärtner J, Möbius W, Nave KA, Saher G. 2019. Ketogenic diet ameliorates axonal defects and promotes myelination in Pelizaeus-Merzbacher disease. *Acta Neuropathologica* **138**:147–161. DOI: <https://doi.org/10.1007/s00401-019-01985-2>, PMID: 30919030
- Susuki K**, Zollinger DR, Chang KJ, Zhang C, Huang CY, Tsai CR, Galiano MR, Liu Y, Benusa SD, Yermakov LM, Griggs RB, Dupree JL, Rasband MN. 2018. Glial βii spectrin contributes to paranode formation and maintenance. *Journal of Neuroscience* **38**:6063–6075. DOI: <https://doi.org/10.1523/JNEUROSCI.3647-17.2018>, PMID: 29853631
- Tait S**, Gunn-Moore F, Collinson JM, Huang J, Lubetzki C, Pedraza L, Sherman DL, Colman DR, Brophy PJ. 2000. An oligodendrocyte cell adhesion molecule at the site of assembly of the paranodal axo-glial junction. *The Journal of Cell Biology* **150**:657–666. DOI: <https://doi.org/10.1083/jcb.150.3.657>, PMID: 10931875
- Taveggia C**, Zanazzi G, Petrylak A, Yano H, Rosenbluth J, Einheber S, Xu X, Esper RM, Loeb JA, Shrager P, Chao MV, Falls DL, Role L, Salzer JL. 2005. Neuregulin-1 type III determines the ensheathment fate of axons. *Neuron* **47**:681–694. DOI: <https://doi.org/10.1016/j.neuron.2005.08.017>, PMID: 16129398
- Thakurela S**, Garding A, Jung RB, Müller C, Goebels S, White R, Werner HB, Tiwari VK. 2016. The transcriptome of mouse central nervous system myelin. *Scientific Reports* **6**:25828. DOI: <https://doi.org/10.1038/srep25828>, PMID: 27173133
- Tokuda N**, Noto Y, Kitani-Morii F, Hamano A, Kasai T, Shiga K, Mizuta I, Niwa F, Nakagawa M, Mizuno T. 2015. Parasympathetic dominant autonomic dysfunction in Charcot-Marie-Tooth disease type 2J with the MPZ Thr124Met Mutation. *Internal Medicine* **54**:1919–1922. DOI: <https://doi.org/10.2169/internalmedicine.54.4259>, PMID: 26234237
- Tokunaga S**, Hashiguchi A, Yoshimura A, Maeda K, Suzuki T, Haruki H, Nakamura T, Okamoto Y, Takashima H. 2012. Late-onset Charcot-Marie-Tooth disease 4F caused by periaxin gene mutation. *Neurogenetics* **13**:359–365. DOI: <https://doi.org/10.1007/s10048-012-0338-5>, PMID: 22847150
- Trapp BD**, Dubois-Dalcq M, Quarles RH. 1984. Ultrastructural localization of P2 protein in actively myelinating rat Schwann cells. *Journal of Neurochemistry* **43**:944–952. DOI: <https://doi.org/10.1111/j.1471-4159.1984.tb12828.x>, PMID: 6206203
- Triolo D**, Dina G, Taveggia C, Vaccari I, Porrello E, Rivellini C, Domi T, La Marca R, Cerri F, Bolino A, Quattrini A, Previtali SC. 2012. Vimentin regulates peripheral nerve myelination. *Development* **139**:1359–1367. DOI: <https://doi.org/10.1242/dev.072371>, PMID: 22357929

- Verheijen MH**, Chrast R, Burrola P, Lemke G. 2003. Local regulation of fat metabolism in peripheral nerves. *Genes & Development* **17**:2450–2464. DOI: <https://doi.org/10.1101/gad.1116203>, PMID: 14522948
- Vizcaino JA**, Csordas A, del-Toro N, Dianas JA, Griss J, Lavidas I, Mayer G, Perez-Riverol Y, Reisinger F, Ternent T, Xu QW, Wang R, Hermjakob H. 2016. Update of the PRIDE database and its related tools. *Nucleic Acids Research* **44**:D447–D456. DOI: <https://doi.org/10.1093/nar/gkv1145>, PMID: 26527722
- Weil MT**, Heibeck S, Töpperwien M, Tom Dieck S, Ruhwedel T, Salditt T, Rodicio MC, Morgan JR, Nave KA, Möbius W, Werner HB. 2018. Axonal ensheathment in the nervous system of lamprey: implications for the evolution of myelinating glia. *Journal of Neuroscience* **38**:6586–6596. DOI: <https://doi.org/10.1523/JNEUROSCI.1034-18.2018>, PMID: 29941446
- Werner HB**, Kuhlmann K, Shen S, Uecker M, Schardt A, Dimova K, Orfaniotou F, Dhaunchak A, Brinkmann BG, Möbius W, Guarente L, Casaccia-Bonnel P, Jahn O, Nave KA. 2007. Proteolipid protein is required for transport of sirtuin 2 into CNS myelin. *Journal of Neuroscience* **27**:7717–7730. DOI: <https://doi.org/10.1523/JNEUROSCI.1254-07.2007>, PMID: 17634366
- Whitaker JN**. 1981. The protein antigens of peripheral nerve myelin. *Annals of Neurology* **9**:56–64. DOI: <https://doi.org/10.1002/ana.410090710>, PMID: 6164338
- Woldeyesus MT**, Britsch S, Riethmacher D, Xu L, Sonnenberg-Riethmacher E, Abou-Rebyeh F, Harvey R, Caroni P, Birchmeier C. 1999. Peripheral nervous system defects in erbB2 mutants following genetic rescue of heart development. *Genes & Development* **13**:2538–2548. DOI: <https://doi.org/10.1101/gad.13.19.2538>, PMID: 10521398
- Yamada H**, Shimizu T, Tanaka T, Campbell KP, Matsumura K. 1994. Dystroglycan is a binding protein of laminin and merosin in peripheral nerve. *FEBS Letters* **352**:49–53. DOI: [https://doi.org/10.1016/0014-5793\(94\)00917-1](https://doi.org/10.1016/0014-5793(94)00917-1), PMID: 7925941
- Yang D**, Bierman J, Tarumi YS, Zhong YP, Rangwala R, Proctor TM, Miyagoe-Suzuki Y, Takeda S, Miner JH, Sherman LS, Gold BG, Patton BL. 2005. Coordinate control of axon defasciculation and myelination by laminin-2 and -8. *Journal of Cell Biology* **168**:655–666. DOI: <https://doi.org/10.1083/jcb.200411158>, PMID: 15699217
- Zhang Y**, Chen K, Sloan SA, Bennett ML, Scholze AR, O’Keeffe S, Phatnani HP, Guarnieri P, Caneda C, Ruderisch N, Deng S, Liddelow SA, Zhang C, Daneman R, Maniatis T, Barres BA, Wu JQ. 2014. An RNA-sequencing transcriptome and splicing database of glia, neurons, and vascular cells of the cerebral cortex. *Journal of Neuroscience* **34**:11929–11947. DOI: <https://doi.org/10.1523/JNEUROSCI.1860-14.2014>, PMID: 25186741